Towards simplified and optimized a posteriori error estimation using PGD reduced models

Pierre-Eric Allier, Ludovic Chamoin, Pierre Ladevèze

Towards simplified and optimized a posteriori error estimation using PGD reduced models

Pierre-Eric Allier | Ludovic Chamoin | Pierre Ladevèze

LMT, ENS Cachan, CNRS, Université Paris-Saclay, 61 Avenue du Président Wilson, 94230 Cachan, France

Correspondence
Ludovic Chamoin, LMT, ENS Cachan, CNRS, Université Paris-Saclay, 61 Avenue du Président Wilson, 94230 Cachan, France.
Email: chamoin@ens-paris-saclay.fr

Summary

The paper deals with the use of model order reduction within a posteriori error estimation procedures in the context of the finite element method. More specifically, it focuses on the constitutive relation error concept, which has been widely used over the last 40 years for FEM verification of computational mechanics models. A technical key-point when using constitutive relation error is the construction of admissible fields, and we propose here to use the proper generalized decomposition to facilitate this task. In addition to making the implementation into commercial FE software easier, it is shown that the use of proper generalized decomposition enables to optimize the verification procedure and to get both accurate and reasonably expensive upper bounds on the discretization error. Numerical illustrations are presented to assess the performance of the proposed approach.

KEYWORDS

constitutive relation error, error estimation, finite element methods, model reduction, proper generalized decomposition

1 | INTRODUCTION

Numerical models, such as these obtained using the finite element method (FEM), are fundamental in science and engineering activities as they constitute the basic ingredient of simulations that enable to predict the behavior of physical phenomena. Consequently, a permanent issue is the verification of these models, which nowadays can attain very high levels of complexity, to certify the quality of numerical simulations. Model verification deals with the assessment of the numerical (FE) model with respect to an initial mathematical model and implies the estimation of discretization error to control the quality of the approximate numerical solution. It delivers error estimates that can further be used in mesh adaptivity processes. In this context, a large set of a posteriori error estimates has appeared over the last 30 years (see previous studies[1-4] for an overview). Methods can be roughly classified in 3 categories: (1) those based on field smoothing (initiated in Zienkiewicz and Zhu[5]); (2) those based on residuals of equilibrium (initiated in Babuška and Rheinboldt[6]); and (3) those based on residuals of the constitutive relation (initiated in Ladevèze and Leguillon[7]). In this work, we focus on the latter methods that involve the constitutive relation error (CRE) concept.

In the context of Computational Mechanics models in which the constitutive relation is a major component, the CRE concept is a convenient and powerful tool. The idea of CRE is rather simple: so-called admissible fields verifying all equations of the model except the constitutive relation are constructed, then the residual associated with the constitutive relation is measured. The CRE concept was first introduced as a robust a posteriori error estimator in FE computations,[8] enabling to compute both strict and effective discretization error bounds for linear and more generally

convex Structural Mechanics problems and to lead mesh adaptivity processes. It was primarily used for linear thermal and elasticity problems[7,9] before being extended to nonlinear time-dependent problems[10,11] and to goal-oriented error estimation.[12-15] The use of CRE for model verification, for which a general overview can be found in other works,[3,16] requires in particular the computation of admissible dual fields that are fully equilibrated. This requirement, which is the main practical issue both in terms of computational cost and implementation technicality, was addressed by means of several techniques[3,7,17-29]; we concentrate here on the hybrid-flux approach, referred as *Element Equilibration Technique* (EET) in the recent literature, that post-processes the primal FE solution at hand and requires local fine-scale computations.

The objective of the paper is to present new numerical tools, on the basis of model reduction techniques and an offline/online strategy that can be coupled to the CRE concept to make this latter fully implementable and exploitable for practical industrial applications. They particularly aim at decreasing the computational cost and technicality level, which are required when computing admissible fields, leading to fast and inexpensive V&V procedures. For that purpose, we decide to refer to the proper generalized decomposition (PGD), which is an a priori model reduction technique that has been extensively used over the last decade to solve multiparametric problems (see previous works[30-33]).

First, starting from the classical hybrid-flux approach, we introduce a reduced model at the element level issued from a parameterization of local problems. This approach, later referred as EET-PGD, was primarily introduced in Chamoin et al[34] for a simple case (it is generalized here). It leads to a precomputation of local equilibrium from given data (tractions, element geometry, and material), in an offline step, using PGD. The PGD solution is then used and post-processed in the online step. Second, from the PGD representation mentioned previously, we address optimization of tractions (or hybrid fluxes) by introducing dual unknowns over each element of the mesh. A global optimization problem is thus defined for which all expensive computations (such as numerical integrations) can be performed in the offline step. The associated technique is later referred as HFT-PGD where HFT stands for *Hybrid Flux Technique*, as equilibration at the element level is indirectly performed here.

In the context of model verification, the CRE concept was already used to control PGD approximations (see a posteriori error estimates developed in other studies[35,36]) or to directly drive the PGD process with CRE minimization.[37] Nevertheless, the use of PGD in CRE implementation has never been investigated and we wish to show here that there are major advantages to do so, in particular for the construction of equilibrated fields. The goal is to give a general framework on the effective use of PGD for model verification with CRE. For the sake of simplicity and clarity, we consider scalar linear elliptic (stationary thermal) problems to introduce technicalities of the proposed approach, but extensions to elasticity, time-dependent, or nonlinear problems are also given with regard to existing literature[3,10]).

The paper outline is as follows: We review in Section 2 the CRE concept and classical construction of equilibrated fields for a general nonlinear mechanical problem; the use of PGD in addition to CRE for the construction of admissible fields (EET-PGD technique) is shown in detail in Section 3; optimization of tractions using PGD (HFT-PGD technique) is addressed in Section 4; illustrative numerical results are reported in Section 5; eventually, conclusions are drawn in Section 6.

2 | MODEL PROBLEM AND A POSTERIORI ERROR ESTIMATION WITH CRE

2.1 | Model problem

We consider a structure that occupies a continuum open bounded domain $\Omega \subset \mathbb{R}^d$ with boundary $\partial\Omega$. We consider small displacements, quasi-static loadings, and isothermal conditions. The time interval is denoted by $[0, T]$. The structure, for all $t \in [0, T]$, is placed in an environment characterized by a given displacement $\boldsymbol{u}_d$ on $\partial_1\Omega \subset \partial\Omega$, given tractions $\boldsymbol{F}_d$ on $\partial_2\Omega$, and a given body force $\boldsymbol{f}_d$ in Ω. $\partial_1\Omega$ and $\partial_2\Omega$ are complementary parts of $\partial\Omega$. The problem that describes the evolution of the structure on $[0, T]$ is to find the displacement-stress pair $(\boldsymbol{u}, \boldsymbol{\sigma})$ that verifies the following:

- kinematic constraints

$$\boldsymbol{u} \in \mathcal{U}^{[0,T]} \quad ; \quad \boldsymbol{u}_{|\partial_1\Omega} = \boldsymbol{u}_d \quad \forall t \in]0, T[\quad ; \quad \epsilon(\boldsymbol{u}) = \frac{1}{2}(\nabla \boldsymbol{u} + \nabla^T \boldsymbol{u}), \tag{1}$$

- equilibrium equations (principle of virtual works)

$$\boldsymbol{\sigma} \in \mathcal{S}^{[0,T]} \quad ; \quad \int_\Omega \boldsymbol{\sigma} : \epsilon(\boldsymbol{u}^*) = \int_\Omega \boldsymbol{f}_d \boldsymbol{u}^* + \int_{\partial_2\Omega} \boldsymbol{F}_d \boldsymbol{u}^* \quad \forall \boldsymbol{u}^* \in \mathcal{U}_0, \forall t \in]0, T[, \tag{2}$$

- constitutive relations

$$\sigma\sigma_t = \mathcal{A}(\epsilon(\dot{\boldsymbol{u}})_{|\tau}, 0 \leq \tau \leq t) \quad \forall(\boldsymbol{x}, t) \in \Omega\times]0, T[. \tag{3}$$

$\mathcal{U}^{[0,T]} = L^2([0,T]; [H^1(\Omega)]^d)$ is the space containing the displacement field $\boldsymbol{u}$ defined on $\Omega\times]0,T[$. $\mathcal{S}^{[0,T]} = L^2([0,T]; H(div,\Omega))$ is the space of symmetric tensors containing the stress field $\boldsymbol{\sigma}$ defined on $\Omega\times]0,T[$. $\mathcal{U}_0$ is the vector space of specified virtual displacements. The operator $\mathcal{A}$ characterizes the mechanical behavior of the material; it may be nonlinear and dependent on history.

Let us denote by $\mathcal{U}_{ad}^{[0,T]} \subset \mathcal{U}^{[0,T]}$ the space of displacements verifying the kinematic constraints (1), and $\mathcal{S}_{ad}^{[0,T]} \subset \mathcal{S}^{[0,T]}$ the space of stress fields, which are solutions to equilibrium equation 2.

2.2 | The CRE concept

2.2.1 | General idea

The CRE concept is built from a dual approach and measures the residual on the constitutive relation; it is a robust error estimate in the context of model verification.

The notion of error in the constitutive law (CRE) was introduced in Ladevèze and Leguillon.[7] The general concept is to split the equations of the problem into two groups with different mechanical contents. The first group involves "safe" equations, ie, kinematic and static constraints whereas the second group involves less reliable equations, ie, constitutive relation equations. A solution satisfying the first group is called admissible. An admissible solution is the exact solution to the problem if and only if it satisfies the equations of the second group. Thus, the quality of the admissible solution may be evaluated through the residuals associated to the equations of the second group. Since the second group is related to the constitutive relations, the terminology of error in the constitutive law was naturally introduced. The splitting of the equations into the two groups is not always obvious. For instance, when the material behavior is described using internal variables, the state laws may be seen as "internal" equilibrium relations and thus included in the first group, or seen as constitutive law like the evolution laws and thus included in the second group. The first choice was investigated in Ladevèze and Moës.[10] This choice leads to the terminology of dissipation error since the error is measured through the residuals of the sole evolution laws, the state laws being a priori satisfied. An alternative is to consider the state laws as part of the second group; in this case, the error estimate involves the residuals associated to both the state and evolution laws. We shall see that this second choice allows to fit elasticity, plasticity, and viscoplasticity with or without softening in the same framework. The dissipation error is recovered as a particular case by enforcing strongly the state laws.

The CRE definition is based on duality pairing. Constitutive relation error gives guaranteed bounds on a large set of problems. In the following, we give examples of CRE functionals for classical mechanical models.

2.2.2 | Linear elasticity

Let us start with the simplest family of problems, ie, elasticity problems. One looks for the final state of the structure at $t = T$, and the problem does not depend on time. The constitutive relation reads

$$\boldsymbol{\sigma} = \mathcal{K}\epsilon(\boldsymbol{u}), \tag{4}$$

where $\mathcal{K}$ is the Hooke tensor, which is symmetric and positive definite. The admissibility spaces are denoted $\mathcal{U}_{ad}$ and $\mathcal{S}_{ad}$. An FE solution $(\boldsymbol{u}_h, \boldsymbol{\sigma}_h)$ is computed, where $\sigma\sigma_h = \mathcal{K}\epsilon(\boldsymbol{u}_h)$ is equilibrated in the finite element sense.

The principle is to associate a new displacement-stress pair denoted $(\hat{\boldsymbol{u}}, \hat{\boldsymbol{\sigma}})$, which is admissible, ie, in $\mathcal{U}_{ad} \times \mathcal{S}_{ad}$. The pair verifies the most reliable equations of the problem; its quality and that of the FE solution is measured through the residual related to the constitutive relation. The crucial point is to build a stress $\hat{\boldsymbol{\sigma}}$ that verifies equilibrium equations. Once $(\hat{\boldsymbol{u}}, \hat{\boldsymbol{\sigma}})$ is obtained, the constitutive relation error reads

$$E_{CRE}^2(\hat{\boldsymbol{u}}, \hat{\boldsymbol{\sigma}}) = \int_\Omega [\psi(\epsilon(\hat{\boldsymbol{u}})) + \psi^*(\hat{\boldsymbol{\sigma}}) - \hat{\boldsymbol{\sigma}} : \epsilon(\hat{\boldsymbol{u}})] = \frac{1}{2}\|\hat{\boldsymbol{\sigma}} - \mathcal{K}\epsilon(\hat{\boldsymbol{u}})\|_{\mathcal{S}}^2, \tag{5}$$

where $\|\cdot\|_{\mathcal{S}} = \sqrt{\int_\Omega \cdot\, \mathcal{K}^{-1} \cdot}$ is the energy norm. $\psi(\epsilon(\hat{\boldsymbol{u}})) = \frac{1}{2}\mathcal{K}\epsilon(\hat{\boldsymbol{u}}) : \epsilon(\hat{\boldsymbol{u}})$ and $\psi^*(\hat{\boldsymbol{\sigma}}) = \frac{1}{2}\mathcal{K}^{-1}\hat{\boldsymbol{\sigma}} : \hat{\boldsymbol{\sigma}}$ are dual (in the Legendre Fenchel sense) convex potentials related to free energy. This error estimate is related to the error defined from

the exact solution through the Prager-Synge theorem:

$$\|\hat{\boldsymbol{u}} - \boldsymbol{u}\|_{\mathcal{U}}^2 + \|\hat{\boldsymbol{\sigma}} - \boldsymbol{\sigma}\|_S^2 = 2E_{CRE}^2(\hat{\boldsymbol{u}}, \hat{\boldsymbol{\sigma}}). \tag{6}$$

2.2.3 | Viscoplasticity

We consider materials with standard thermodynamics formulation involving internal variables and small displacements without softening such as viscoplasticity.[3,10,12] The reference problem is reformulated introducing internal variables (rather than formulating the constitutive relation in functional form). Internal variables other than the plastic strain tensor ϵ_p (such as the accumulated plastic strain p for isotropic hardening) are gathered in a vector $\mathbb{X}$. The force associated to $\mathbb{X}$, involving the additional yield stress R for isotropic hardening, is denoted $\mathbb{Y}$, and we introduce quantities $\boldsymbol{s} = (\boldsymbol{\sigma}, \mathbb{Y})^T$, $\dot{\boldsymbol{e}}_p = (\dot{\epsilon}_p, -\dot{\mathbb{X}})^T$, and $\dot{\boldsymbol{e}}_e = (\dot{\epsilon}_e, \dot{\mathbb{X}})^T$, so that the dissipation reads $d = \int_0^T \int_\Omega \boldsymbol{s} \cdot \dot{\boldsymbol{e}}_p$. The material behavior is described by state equations $\boldsymbol{e}_e = \Lambda(\boldsymbol{s}) = \frac{\partial \Psi^*}{\partial \boldsymbol{s}}$ (or $\boldsymbol{s} = \frac{\partial \Psi}{\partial \boldsymbol{e}_e}$), where Ψ and Ψ^* are free energy potentials, and evolution laws $\dot{\boldsymbol{e}}_p = B(\boldsymbol{s})$. Λ is assumed to be linear, symmetric, and positive; this is the case of most viscoplastic materials, after a change of variables (normal description). B can be nonlinear and multivalued, as in plasticity; it is assumed to be expressed with two pseudo-potentials of dissipation φ and φ^* that are dual convex functions (family of standard materials): $\dot{\boldsymbol{e}}_p \in \partial_{\boldsymbol{s}} \varphi^*(\boldsymbol{s})$ with $\partial_{\boldsymbol{s}}$ denoting subdifferentials; these correspond to the indicatrix function of the elasticity domain for plasticity problems.

The equations of the problem are then divided in two groups:

- The first one related to the free energy defines the admissibility and combines equilibrium equations ($\boldsymbol{s}$ is S-admissible), kinematic constraints ($\dot{\boldsymbol{e}} = \dot{\boldsymbol{e}}_e + \dot{\boldsymbol{e}}_p$ is K-admissible), initial conditions ($\boldsymbol{e}_p = 0$ at $t = 0$), and state equations; and
- The second group, related to dissipation, only includes evolution laws.

The quality of an admissible solution is estimated through the quality of satisfaction of the evolution laws. This defines the CRE error of dissipation type, for which there is a link (similar to the Prager-Synge theorem) with the solution error:

$$E_{CRE}^2(\dot{\hat{\boldsymbol{e}}}_p, \hat{\boldsymbol{s}}) = \int_0^T \int_\Omega e_{CRE}^2(\dot{\hat{\boldsymbol{e}}}_p, \hat{\boldsymbol{s}}) \quad ; \quad e_{CRE}^2(\dot{\hat{\boldsymbol{e}}}_p, \hat{\boldsymbol{s}}) = \varphi^*(\hat{\boldsymbol{s}}) + \varphi(\dot{\hat{\boldsymbol{e}}}_p) - \hat{\boldsymbol{s}} \cdot \dot{\hat{\boldsymbol{e}}}_p. \tag{7}$$

Remark 1. A more general framework for the dissipation error (7) was proposed in Ladevèze[12] when evolution laws are not given by potentials (but the operator B remains monotonous).

Remark 2. An alternative definition of the CRE functional for nonlinear dissipative models is as follows:

$$E_{CRE}^2(\hat{\boldsymbol{e}}, \hat{\boldsymbol{s}}) = \int_\Omega \left[\Psi^*(\hat{\boldsymbol{s}}) + \Psi(\hat{\boldsymbol{e}}) - \hat{\boldsymbol{s}} \cdot \hat{\boldsymbol{e}}\right]_{|T} + \int_0^T \int_\Omega \left[\varphi^*(\hat{\boldsymbol{s}}) + \varphi(\dot{\hat{\boldsymbol{e}}}_p) - \hat{\boldsymbol{s}} \cdot \dot{\hat{\boldsymbol{e}}}_p\right]. \tag{8}$$

It is based on a definition of admissibility similar to elasticity and involves residuals on both state equations and evolution laws. It is a suitable definition that preserves convexity properties when addressing damage models (softening materials).[11,38]

2.3 | Recovering admissible fields

2.3.1 | Elasticity case

We usually choose $\hat{\boldsymbol{u}} = \boldsymbol{u}_h$. The construction of $\hat{\boldsymbol{\sigma}}$ is more technical, and several methods have been proposed. The optimal method would be a full dual analysis (minimizing the complementary energy using equilibrium elements, see previous studies[39-42]). However, this is hardly applicable in practice, as it requires the solution of an additional global problem, with substantial computational efforts and nonconventional FE spaces that are usually not available in commercial software.

We focus on the hybrid-flux method (or EET) that enables to compute an admissible field $\hat{\boldsymbol{\sigma}}_h \in \mathcal{S}_{ad}$ from a post-processing of the FE field $\boldsymbol{\sigma}_h$ at hand, with local independent computations.[3,7,17] The key is the prolongation condition:

$$\int_K (\hat{\boldsymbol{\sigma}}_h - \boldsymbol{\sigma}_h) \boldsymbol{\nabla} \phi_i = 0, \tag{9}$$

which is enforced for all elements K and all nodes i connected to K. ϕ_i is the scalar shape function associated with node i. The recovery method can be split in two steps:

Step 1: recovery of equilibrated tractions $\widehat{\boldsymbol{F}}_{K|\Gamma}$ defined on edges (or faces in 3D) Γ of each element K, with $\widehat{\boldsymbol{F}}_{K|\Gamma} = \boldsymbol{F}_d$ if $\Gamma \subset \partial_2\Omega$, such that equilibrium at the element level is verified:

$$\int_K \boldsymbol{f}_d \cdot \boldsymbol{u}_R^* + \int_{\partial K} \widehat{\boldsymbol{F}}_K \cdot \boldsymbol{u}_R^* = 0 \quad \forall \boldsymbol{u}_R^* \in \mathcal{U}_R(K), \tag{10}$$

where $\mathcal{U}_R(K)$ denotes the space of rigid body motions on K. The prolongation condition (9) then yields (using $\hat{\boldsymbol{\sigma}}_{h|\partial K} \cdot \boldsymbol{n}_K = \widehat{\boldsymbol{F}}_K$ and $\boldsymbol{\nabla} \cdot \hat{\boldsymbol{\sigma}} + \boldsymbol{f}_d = 0$):

$$\int_{\partial K} \widehat{\boldsymbol{F}}_K \phi_i = \int_K (\boldsymbol{\sigma}_h \boldsymbol{\nabla} \phi_i - \boldsymbol{f}_d \phi_i), \tag{11}$$

and leads to small well-posed systems of equations (over patches of elements connected to each node i), which can be solved explicitly. In practice, tractions are defined as $\widehat{\boldsymbol{F}}_{K|\Gamma} = \eta_K^\Gamma \widehat{\boldsymbol{F}}_\Gamma$, with $\eta_K^\Gamma = \pm 1$, to ensure continuity across element boundaries and are searched as a linear combination of FE shape functions: $\widehat{\boldsymbol{F}}_{K|\Gamma}(\boldsymbol{x}) = \sum_{j \in \mathcal{J}_\Gamma} \widehat{\boldsymbol{F}}_{K|\Gamma}^j \phi_j(\boldsymbol{x})$. $\mathcal{J}_\Gamma$ denotes the set of nodes connected to the edge/face Γ. All technical details on the construction of equilibrated tractions can be found in other works[3,27];

Step 2: local recovery of an equilibrated stress field $\hat{\boldsymbol{\sigma}}_h$, for given tractions $\widehat{\boldsymbol{F}}_K$, over each element K solving the Neumann problem:

$$\int_K \hat{\boldsymbol{\sigma}}_h : \epsilon(\boldsymbol{u}^*) = \int_K \boldsymbol{f}_d \cdot \boldsymbol{u}^* + \int_{\partial K} \widehat{\boldsymbol{F}}_K \cdot \boldsymbol{u}^* \quad \forall \boldsymbol{u}^* \in \mathcal{U}(K), \tag{12}$$

with $\mathcal{U}(K) = [H^1(K)]^d$. A solution to (12) may be obtained analytically, using polynomial functions with sufficiently high degree, provided the source term $\boldsymbol{f}_d$ is polynomial as well.[43] In practice, an alternative approach with numerical solution and higher-order elements is preferred. Indeed, the optimal stress field verifying (12) is the one that minimizes over K the local error estimate $\|\hat{\boldsymbol{\sigma}} - \boldsymbol{\sigma}_h\|_{S,K}$ (or equivalently $\|\hat{\boldsymbol{\sigma}}\|_{S,K}$). Duality arguments show that this is equivalent to taking $\hat{\boldsymbol{\sigma}}_{h|K} = \mathcal{K}\epsilon(\boldsymbol{\rho})$, with $\boldsymbol{\rho} \in \mathcal{U}(K)$ verifying:

$$\int_K \mathcal{K}\epsilon(\boldsymbol{\rho}) : \epsilon(\boldsymbol{u}^*) = \int_K \boldsymbol{f}_d \cdot \boldsymbol{u}^* + \int_{\partial K} \widehat{\boldsymbol{F}}_K \cdot \boldsymbol{u}^* \quad \forall \boldsymbol{u}^* \in \mathcal{U}(K). \tag{13}$$

A numerical approximation of the solution of (13) (defined up to rigid body motions in $\mathcal{U}_R(K)$) can be obtained using the FEM with a single finite element of degree $p+k$, where p denotes the polynomial degree used to compute $\boldsymbol{u}_h$ and k denotes the extra degree. Numerical studies performed in Babuška et al[44] showed that analytical and numerical approaches give similar CRE error estimates choosing $k \geq 3$, even though the flux field is not rigorously equilibrated in each element K with the latter approach. We consider the numerical approach in the remainder of the paper.

Solving (13) is in practice the most costly part in the hybrid-flux method (in particular for 3D applications), as it involves high-order elements and has to be performed for each element K. We wish to use model order reduction to circumvent this issue.

2.3.2 | Time-dependent nonlinear case

The FE solution is computed at time points t_n, considering the classical incremental FEM. Assuming that data are piecewise linear on $[0, T]$, we complete the FE solution on $[0, T]$ and get $(\boldsymbol{u}_h, \boldsymbol{\sigma}_h)$. The stress field $\boldsymbol{\sigma}_h$ is FE equilibrated on $[0, T]$. We usually choose $\hat{u}_h = u_h$ (except when incompressibility needs to be enforced[45]).

The crucial point is to build an admissible stress field. For that purpose, the classical recovery used for elasticity is still used for any time point t_n, then a piecewise linear interpolation is performed. Other internal variables, which are not involved in equilibrium equations, are obtained solving local and explicit minimization problems.

3 | ACCELERATION OF LOCAL RECOVERY USING PGD

3.1 | Scalar problem

For the sake of simplicity, we first consider a scalar problem, ie, a steady-state thermal problem that consists in finding the temperature/flux pair $(u, \boldsymbol{q})$ such that

$$\begin{aligned} & u \in \mathcal{U} \quad ; \quad u = u_d \quad \text{on } \partial_1\Omega \quad \text{(kinematic constraints)} \\ \boldsymbol{q} \in \mathcal{S} \quad ; \quad & \int_\Omega \boldsymbol{q} \cdot \boldsymbol{\nabla} u^* = \int_\Omega f_d u^* + \int_{\partial_2\Omega} F_d u^* \quad \forall u^* \in \mathcal{U}_0 \quad \text{(balance equations)} \\ & \boldsymbol{q} = \mathcal{K}\boldsymbol{\nabla} u \quad \text{(constitutive relation)} \end{aligned} \tag{14}$$

with $\mathcal{U} = H^1(\Omega)$ and $\mathcal{S} = H(div, \Omega) = \{\boldsymbol{\pi} \in [L^2(\Omega)]^d, \boldsymbol{\nabla}\cdot\boldsymbol{\pi} \in L^2(\Omega)\}$. $\mathcal{K}$ is a symmetric positive definite operator (second-order tensor). We introduce the energy semi-norm $\|\cdot\|_{\mathcal{U}} = \sqrt{\int_\Omega \boldsymbol{\nabla}(\cdot)\cdot\mathcal{K}\boldsymbol{\nabla}(\cdot)}$. For an admissible pair $(\hat{u}, \hat{\boldsymbol{q}}) \in \mathcal{U}_{ad} \times \mathcal{S}_{ad}$, the CRE functional is defined as follows:

$$E^2_{CRE}(\hat{u}, \hat{\boldsymbol{q}}) = \frac{1}{2}\int_\Omega (\hat{\boldsymbol{q}} - \mathcal{K}\boldsymbol{\nabla}\hat{u})\cdot\mathcal{K}^{-1}(\hat{\boldsymbol{q}} - \mathcal{K}\boldsymbol{\nabla}\hat{u}) = \frac{1}{2}\|\hat{\boldsymbol{q}} - \mathcal{K}\boldsymbol{\nabla}\hat{u}\|^2_{\mathcal{S}}. \tag{15}$$

It measures the nonverification of the constitutive relation for $(\hat{u}, \hat{\boldsymbol{q}})$ and can be used as an error estimate. Indeed, after computing an FE solution $(u_h, \boldsymbol{q}_h)$, choosing $\hat{u} = u_h$ and constructing $\hat{\boldsymbol{q}}_h \in \mathcal{S}_{ad}$ lead to the Prager-Synge theorem (6) and to the following:

$$\|u_h - u\|_{\mathcal{U}} \leq \sqrt{2} E_{CRE}(u_h, \hat{\boldsymbol{q}}_h). \tag{16}$$

The quality of the estimate depends on that of $\hat{\boldsymbol{q}}_h$.

Classically, $\hat{\boldsymbol{q}}_h$ is constructed using the hybrid-flux approach as described in Section 2.3, with the following two steps and specifying that tractions refer here to normal thermal fluxes on element boundaries:

Step 1: construction of equilibrated tractions $\hat{F}_{K|\Gamma} = \eta^\Gamma_K \hat{F}_\Gamma$ on edges/faces Γ of each element K, such that equilibration at the element level is verified:

$$\int_K f_d + \int_{\partial K} \hat{F}_K = 0. \tag{17}$$

This is performed using the prolongation condition, and tractions are searched as linear combinations of FE shape functions: $\hat{F}_{K|\Gamma}(\boldsymbol{x}) = \sum_{j\in\mathcal{J}_\Gamma} \hat{F}^j_{K|\Gamma}\phi_j(\boldsymbol{x})$ (see Figure 1).

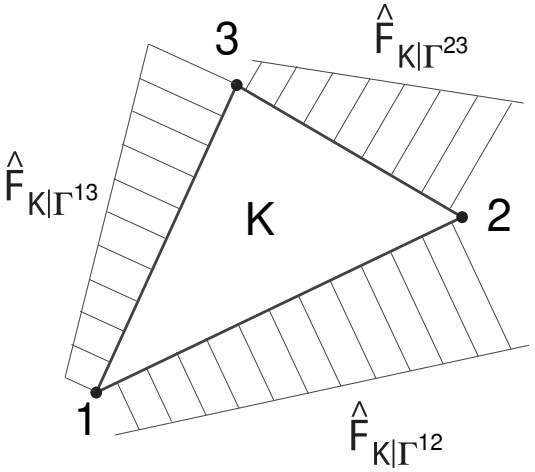

FIGURE 1 Configuration at the level of a 3-node triangle element, with linear tractions $\hat{F}_{K|\Gamma}$ defined on element edges

Step 2: local construction, for given tractions $\hat{F}_K$ and over each element K, of $\hat{\boldsymbol{q}}_{h|K} = \boldsymbol{\mathcal{K}}\boldsymbol{\nabla}\rho$ solving the following local Neumann problem with higher-order elements:

$$\int_K \boldsymbol{\mathcal{K}}\boldsymbol{\nabla}\rho\cdot\boldsymbol{\nabla}u^* = \int_K f_d u^* + \int_{\partial K}\hat{F}_K u^* \quad \forall u^*\in\mathcal{U}(K). \tag{18}$$

Solving (18) is in practice the most costly part in the hybrid-flux method (in particular for 3D applications), as it involves high-order elements and has to be performed for each element K. We wish to use the PGD technique to find, in an offline phase, a parameterized solution to (18), valid for any configuration of the geometry and the loading. From equilibrated tractions computed in step 1 and with respect to problem data (material parameters, mesh geometry, …), this PGD solution would then be directly used in the online error estimation phase, and in a multiquery context, for each element K of the mesh.

3.2 | Parametrization of the local problems

In the following, we consider that the material behavior is isotropic and that material parameters are constant over each element K, so that their values have no influence on $\hat{\boldsymbol{q}}_{h|K}$; we thus set $\boldsymbol{\mathcal{K}} = \mathbb{I}$ when solving (18) and define $\hat{\boldsymbol{q}}_{h|K} = \boldsymbol{\nabla}\rho$. In cases where $\boldsymbol{\mathcal{K}}$ is not constant over each element or is not isotropic, its structure could be parameterized and additional material parameters could be introduced in the PGD decomposition.

On each edge/face Γ of any element K, tractions are linear combinations of FE shape functions and thus read as follows:

$$\hat{F}_{K|\Gamma}(\boldsymbol{x}) = \sum_{j\in\mathcal{J}_\Gamma}\hat{F}^j_{K|\Gamma}\phi_j(\boldsymbol{x}) \quad ; \quad \hat{F}^j_{K|\Gamma} = \eta^\Gamma_K\hat{F}^j_\Gamma \in \mathbb{R}. \tag{19}$$

Consequently, the solution ρ to (18) can be written as a linear combination of elementary solutions:

$$\rho(\boldsymbol{x}) = \sum_{\Gamma\subset\partial K}\sum_{j\in\mathcal{J}_\Gamma}\hat{F}^j_{K|\Gamma}\rho^j_\Gamma(\boldsymbol{x}), \tag{20}$$

where ρ^j_Γ is the solution (up to a constant) to the elementary problem:

$$\int_K \boldsymbol{\nabla}\rho^j_\Gamma\cdot\boldsymbol{\nabla}u^* = \int_\Gamma \phi_j u^* - \int_K\left(\frac{1}{|K|}\int_\Gamma\phi_j\right)u^* \quad \forall u^*\in\mathcal{U}(K). \tag{21}$$

The solution ρ^j_Γ to each problem (21) can be computed with the PGD technique, for any element K, parameterizing the geometry of K with a set of parameters $\boldsymbol{p}_{geo}\in\mathcal{P}$. Following the approach described in other studies,[46-48] we reformulate the weak problem (21) by introducing a parameter-dependent mapping $\mathcal{M}(\boldsymbol{p}_{geo}) : K_{ref}\to K(\boldsymbol{p}_{geo})$ from a reference fixed element K_{ref} to the geometrically parameterized element $K(\boldsymbol{p}_{geo})$. Such a geometrical transformation then allows defining the weak problem in a tensor product space and applying the PGD method, to compute generic parameterized solutions $\rho^j_\Gamma(\boldsymbol{p}_{geo})$ that can be used for any element geometry.

Remark 3. In the presence of geometrical variabilities, an alternative approach described in other works[49,50] could also be used. It consists in embedding the parameterized domain into a fixed fictitious domain.

In the present case, the mapping is defined from two transformations:

- a first scaling mapping $\mathcal{M}_1 : \bar{K}\to K$ maps a homothetic element $\bar{K}$ with diameter 1 to the actual element K with diameter α. This mapping involves a transformation matrix $\mathbb{T}_1 = \alpha\mathbb{I}_d$ such that $\boldsymbol{x} = \mathbb{T}_1\bar{\boldsymbol{x}}$;
- a second mapping $\mathcal{M}_2 : K_{ref}\to\bar{K}$ maps a reference element K_{ref} to element $\bar{K}$. This mapping uses an isoparametric formulation and involves a transformation matrix $\mathbb{T}_2$ such that $\bar{\boldsymbol{x}} = \mathbb{T}_2\boldsymbol{x}_{ref}$.

The global mapping is therefore $\mathcal{M}(\boldsymbol{p}_{geo}) = \mathcal{M}_1\circ\mathcal{M}_2$ with transformation matrix $\mathbb{T}(\boldsymbol{p}_{geo}) = \alpha\mathbb{T}_2$, Jacobian matrix $\mathbb{J} = \mathbb{T}$, and Jacobian $J(\boldsymbol{p}_{geo}) = det(\mathbb{J})$.

As an illustration, we consider two element types. We first consider 3-node triangle elements (Figure 2). The mappings read

$$\begin{pmatrix} \bar{x} \\ \bar{y} \end{pmatrix} = \begin{pmatrix} \sum_{i=1}^{3} \bar{x}_i \phi_i(\eta,\xi) \\ \sum_{i=1}^{3} \bar{y}_i \phi_i(\eta,\xi) \end{pmatrix} = \mathbb{T}_2 \begin{pmatrix} \eta \\ \xi \end{pmatrix} \quad ; \quad \mathbb{T}_2 = \begin{bmatrix} 1 & \bar{x}_3 \\ 0 & \bar{y}_3 \end{bmatrix}, \tag{22}$$

where $(\bar{x}_3, \bar{y}_3)$ are local coordinates of node 3 in the coordinate system associated with element $\bar{K}$ and (η, ξ) are local coordinates in the coordinate system associated with element K_{ref}. The global mapping $\mathcal{M}$ thus involves 3 parameters, ie, $\boldsymbol{p}_{geo} = (\alpha, \bar{x}_3, \bar{y}_3)$ and $J = \alpha^2 \bar{y}_3$.

We now consider 4-node tetrahedron elements (Figure 3). The mappings read

$$\begin{pmatrix} \bar{x} \\ \bar{y} \\ \bar{z} \end{pmatrix} = \begin{pmatrix} \sum_{i=1}^{4} \bar{x}_i \phi_i(\eta,\xi,\tau) \\ \sum_{i=1}^{4} \bar{y}_i \phi_i(\eta,\xi,\tau) \\ \sum_{i=1}^{4} \bar{z}_i \phi_j(\eta,\xi,\tau) \end{pmatrix} = \mathbb{T}_2 \begin{pmatrix} \eta \\ \xi \\ \tau \end{pmatrix} \quad ; \quad \mathbb{T}_2 = \begin{bmatrix} 1 & \bar{x}_3 & \bar{x}_4 \\ 0 & \bar{y}_3 & \bar{y}_4 \\ 0 & 0 & \bar{z}_4 \end{bmatrix}, \tag{23}$$

where $(\bar{x}_3, \bar{y}_3, \bar{x}_4, \bar{y}_4, \bar{z}_4)$ are local coordinates of nodes 3 and 4 in the coordinate system associated with element $\bar{K}$, and (η, ξ, τ) are local coordinates in the coordinate system associated with element K_{ref}. The global mapping $\mathcal{M}$ thus involves 6 parameters, ie, $\boldsymbol{p}_{geo} = (\alpha, \bar{x}_3, \bar{y}_3, \bar{x}_4, \bar{y}_4, \bar{z}_4)$ and $J = \alpha^3 \bar{y}_3 \bar{z}_4$.

Consequently, the problem (21) can be parameterized and defined in a fixed reference element K_{ref} under the form:

$$\int_{K_{ref}} J . \mathbb{J}^{-T} \boldsymbol{\nabla} \rho_{\Gamma}^{j} \cdot \mathbb{J}^{-T} \boldsymbol{\nabla} u^* = \int_{\Gamma_{ref}} J_s \phi_j u^* - \int_{K_{ref}} J . \left(\frac{1}{|K|} \int_{\Gamma_{ref}} J_s \phi_j \right) u^* \quad \forall u^* \in \mathcal{U}(K_{ref}), \tag{24}$$

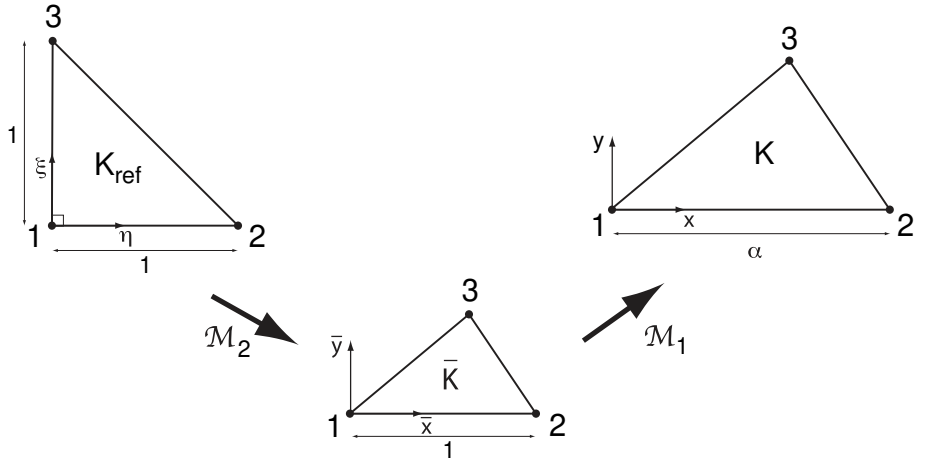

FIGURE 2 Mapping between reference and parameterized elements for a 3-node triangle element

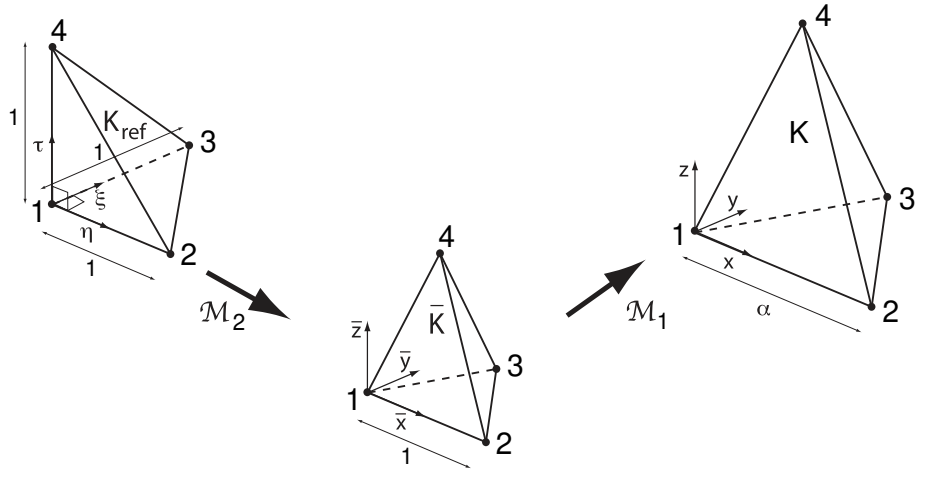

FIGURE 3 Mapping between reference and parameterized elements for a 4-node tetrahedron element

with J_s the Jacobian associated with the transformation of element edge/face Γ. For 3-node triangle elements (Figure 2), it reads

$$J_s = \alpha \begin{cases} 1 & \text{on } \Gamma^{12} \\ \sqrt{(1-\bar{x}_3)^2 + \bar{y}_3^2} & \text{on } \Gamma^{23} \\ \sqrt{\bar{x}_3^2 + \bar{y}_3^2} & \text{on } \Gamma^{13} \end{cases}, \tag{25}$$

whereas for 4-node tetrahedron elements (Figure 3), it reads

$$J_s = \alpha^2 \begin{cases} \bar{y}_3 & \text{on } \Gamma^{123} \\ \sqrt{\bar{y}_4^2 + \bar{z}_4^2} & \text{on } \Gamma^{124} \\ \sqrt{\bar{z}_4^2(\bar{x}_3^2 + \bar{y}_3^2) + (\bar{x}_4\bar{y}_3 - \bar{x}_3\bar{y}_4)^2} & \text{on } \Gamma^{134} \\ \sqrt{\bar{z}_4^2((\bar{x}_3-1)^2 + \bar{y}_3^2) + ((\bar{x}_4-1)\bar{y}_3 - (\bar{x}_3-1)\bar{y}_4)^2} & \text{on } \Gamma^{234} \end{cases}. \tag{26}$$

Remark 4. Equivalently, (24) can be recast as follows:

$$\int_{K_{ref}} \boldsymbol{\nabla} \rho_\Gamma^j \cdot \tilde{\mathbb{K}} \boldsymbol{\nabla} u^* = \int_{\Gamma_{ref}} \tilde{F}_d \, u^* + \int_{K_{ref}} \tilde{f}_d \, u^* \quad \forall u^* \in \mathcal{U}(K_{ref}), \tag{27}$$

with $\tilde{\mathbb{K}} = J.\mathbb{J}^{-1}\mathbb{J}^{-T}$, $\tilde{F}_d = J_s\phi_j$, and $\tilde{f}_d = -J.\left(\frac{1}{|K|}\int_{\Gamma_{ref}} J_s\phi_j\right)$.

Remark 5. The number of elementary problems (21) (or (24)) and the number of parameters involved in the mapping $\mathcal{M}$ (size of $\boldsymbol{p}_{geo}$) depend on the type of FE element. For instance,

- 3-node triangle elements involve 6 elementary problems (2 for each of the 3 edges) and 3 geometrical parameters (6 degrees of freedom with 3 rigid body motions);
- 6-node triangle elements involve 9 elementary problems (3 for each of the 3 edges) and 9 geometrical parameters (12 degrees of freedom with 3 rigid body motions);
- 4-node tetrahedron elements involve 12 elementary problems (3 for each of the 4 faces) and 6 geometrical parameters (12 degrees of freedom with 6 rigid body motions).

3.3 | Solution using PGD

We now introduce a reduced model, based on PGD, at the element level to facilitate step 2 of the hybrid-flux approach. For that purpose, approximations of solutions $\rho_\Gamma^j(\boldsymbol{x}_{ref}, \boldsymbol{p}_{geo})$ are computed offline and once for all using the PGD technique with separated-variable modal decomposition.

Considering a general linear D-dimensional problem defined on the tensor space $\mathcal{X} = \mathcal{X}_1 \otimes \mathcal{X}_2 \otimes \cdots \otimes \mathcal{X}_D$, PGD is a low-rank tensor method that consists in searching an approximation u_m of u in a low-dimensional tensor subspace of $\mathcal{X}_m \subset \mathcal{X}$ made of canonical format tensors of rank m:

$$u_m = \sum_{i=1}^{m} w_i^1 \otimes w_i^2 \cdots \otimes w_i^D \quad , \quad w_i^\mu \in \mathcal{X}_\mu. \tag{28}$$

Among the various strategies to construct u_m,[51] we focus on the one called *progressive Galerkin*. Introducing a global weak formulation of the problem,

$$\text{find} \quad u \in \mathcal{X} \text{ such that } B(u,v) = F(v) \quad \forall v \in \mathcal{X}, \tag{29}$$

and assuming that the rank $m-1$ decomposition u_{m-1} is known, the rank m decomposition $u_m = u_{m-1} + w^1 \otimes w^2 \cdots \otimes w^D$ is searched such that

$$B(u_m, \delta v) = F(\delta v) \quad \forall \delta v = \delta w^1 \otimes w^2 \cdots \otimes w^D + w^1 \otimes \delta w^2 \cdots \otimes w^D + \cdots + w^1 \otimes w^2 \cdots \otimes \delta w^D, \tag{30}$$

with $\delta w^\mu \in \mathcal{X}_\mu$. This formulation naturally leads to a nonlinear problem where a set of coupled low-dimensional problems have to be solved:

$$\begin{aligned}
B(w^1 \otimes w^2 \cdots \otimes w^D, \delta w^1 \otimes w^2 \cdots \otimes w^D) &= R_{m-1}(\delta w^1 \otimes w^2 \cdots \otimes w^D) \quad \forall \delta w^1 \in \mathcal{X}_1, \\
B(w^1 \otimes w^2 \cdots \otimes w^D, w^1 \otimes \delta w^2 \cdots \otimes w^D) &= R_{m-1}(w^1 \otimes \delta w^2 \cdots \otimes w^D) \quad \forall \delta w^2 \in \mathcal{X}_2, \\
&\vdots = \vdots \\
B(w^1 \otimes w^2 \cdots \otimes w^D, w^1 \otimes w^2 \cdots \otimes \delta w^D) &= R_{m-1}(w^1 \otimes w^2 \cdots \otimes \delta w^D) \quad \forall \delta w^D \in \mathcal{X}_D,
\end{aligned} \tag{31}$$

with $R_{m-1}(v) = F(v) - B(u_{m-1}, v)$. This problem is in practice solved using alternated minimization with an iterative (fixed point) strategy.

To solve (24) with the progressive Galerkin approach of PGD, we introduce the following bilinear form B and linear form F constructed from the parameterized separated variable Jacobian transformation (all technical details can be found in other works[46,47]). Introducing the interval $I_{p^k_{geo}}$ in which parameter p^k_{geo} evolves ($1 \leq k \leq P = size(\boldsymbol{p}_{geo})$), these forms read

$$\begin{aligned}
B(\rho^j_\Gamma, v) &= \int_{I_\alpha} \int_{I_{p_{geo,1}}} \cdots \int_{I_{p_{geo,P}}} \int_{K_{ref}} J_. \mathbb{J}^{-T} \boldsymbol{\nabla} \rho^j_\Gamma \cdot \mathbb{J}^{-T} \boldsymbol{\nabla} v, \\
F(v) &= \int_{I_\alpha} \int_{I_{p_{geo,1}}} \cdots \int_{I_{p_{geo,P}}} \left[\int_{\Gamma_{ref}} J_s \phi_j v - \int_{K_{ref}} J_. \left(\frac{1}{|K|} \int_{\Gamma_{ref}} J_s \phi_j \right) v \right].
\end{aligned} \tag{32}$$

The parameter α is included only for completeness of the description; it acts as a multiplicative constant in the solution ρ and disappears when computing $\hat{\boldsymbol{q}}_{h|K} = \mathcal{K} \boldsymbol{\nabla} \rho$. PGD solutions thus read

$$\rho^j_{\Gamma,m}(\boldsymbol{x}_{ref}, \boldsymbol{p}_{geo}) = \alpha \sum_{i=1}^{m} \left(\psi_i(\boldsymbol{x}_{ref}) \prod_{2 \leq k \leq P} \delta_i^{p_{geo,k}}(p_{geo,k}) \right). \tag{33}$$

Space functions $\psi_i(\boldsymbol{x}_{ref})$ in (33) are computed using the FEM with a single element of degree $p + k$. Other functions are discretized using a fine grid over individual spaces $I_{p_{geo,k}}$. Additionally, square roots involved in J_s are approximated using SVD and polynomial interpolation with high degree (degree 8 in practice).

Remark 6. The number m of PGD modes that is required to get accurate solutions $\rho^j_{\Gamma,m}$ can be rigorously defined using classical a posteriori error estimation tools devoted to PGD.[35,36,52,53] For extremal cases (elements with bad shape), the number of PGD modes should be chosen carefully; however, too much distorted elements are usually avoided in practice (regular meshes) and a few number of PGD modes leads to a PGD error, which is negligible compared to the discretization error that we wish to assess. A numerical evaluation of the value m that yields sufficient accuracy is provided in the numerical results.

Combining (20) and (33), a PGD representation of $\rho(\boldsymbol{x})$ solution to (18) reads

$$\rho_m(\boldsymbol{x}_{ref}, \boldsymbol{p}_{geo}, \{\hat{F}^j_{K|\Gamma}\}) = \sum_{\Gamma \subset \partial K} \sum_{j \in \mathcal{J}_\Gamma} \hat{F}^j_{K|\Gamma} \rho^j_{\Gamma,m}(\boldsymbol{x}_{ref}, \boldsymbol{p}_{geo}). \tag{34}$$

It provides for a parameterized equilibrated flux field at the element level:

$$\hat{\boldsymbol{q}}_{h,m|K}(\boldsymbol{x}_{ref}, \boldsymbol{p}_{geo}, \{\hat{F}^j_{K|\Gamma}\}) = \mathbb{J}^{-T}(\boldsymbol{p}_{geo}) \boldsymbol{\nabla} \left(\sum_{\Gamma \subset \partial K} \sum_{j \in \mathcal{J}_\Gamma} \hat{F}^j_{K|\Gamma} \rho^j_{\Gamma,m}(\boldsymbol{x}_{ref}, \boldsymbol{p}_{geo}) \right), \tag{35}$$

which can be directly used online in the a posteriori error estimation procedure.

A representation of the use of PGD in step 2 of the hybrid-flux approach (so-called EET-PGD technique) is given in Figure 4.

Remark 7. In practice, the numerical implementation of the EET-PGD technique is organized so that the loop over all elements of the mesh is avoided. It is rather chosen to store all PGD space modes in a single vector and to perform global matrix multiplications which are optimized in classical software.

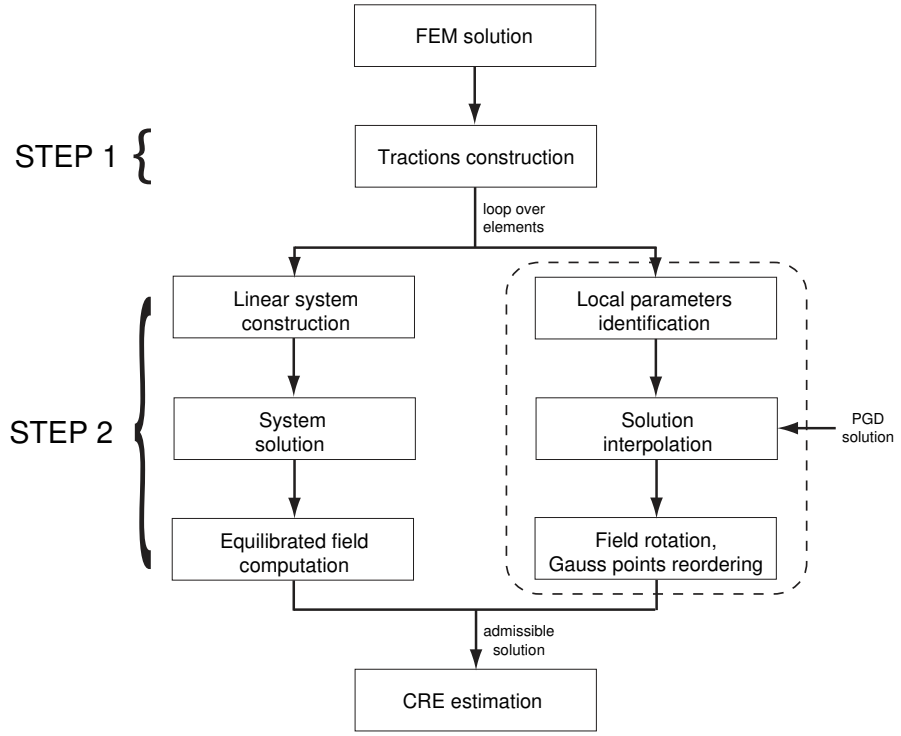

FIGURE 4 Flow chart of the hybrid-flux approach without (left) or with (right) the use of EET-PGD in step 2. CRE, constitutive relation error; EET, Element Equilibration Technique; PGD, proper generalized decomposition

3.4 | Extension to elasticity problems

Considering elasticity problems, the local Neumann problems to solve in step 2 read

$$\int_K \mathcal{K}\epsilon(\boldsymbol{\rho}) : \epsilon(\boldsymbol{u}^*) = \int_K \boldsymbol{f}_d \cdot \boldsymbol{u}^* + \int_{\partial K} \widehat{\boldsymbol{F}}_K \cdot \boldsymbol{u}^* \quad \forall \boldsymbol{u}^* \in \mathcal{U}(K), \tag{36}$$

where $\mathcal{K}$ is the fourth-order symmetric elasticity tensor. On each edge/face Γ of any element K, tractions are linear combinations of FE shape functions and thus read (in the 3D case)

$$\widehat{\boldsymbol{F}}_{K|\Gamma}(\boldsymbol{x}) = \sum_{j\in\mathcal{J}_\Gamma} [\hat{F}^{jx}_{K|\Gamma}\boldsymbol{\phi}^x_j(\boldsymbol{x}) + \hat{F}^{jy}_{K|\Gamma}\boldsymbol{\phi}^y_j(\boldsymbol{x}) + \hat{F}^{jz}_{K|\Gamma}\boldsymbol{\phi}^z_j(\boldsymbol{x})] \quad ; \quad (\hat{F}^{jx}_{K|\Gamma}, \hat{F}^{jy}_{K|\Gamma}, \hat{F}^{jz}_{K|\Gamma})^T = \eta^\Gamma_K(\hat{F}^{jx}_\Gamma, \hat{F}^{jy}_\Gamma, \hat{F}^{jz}_\Gamma)^T \in \mathbb{R}^3, \tag{37}$$

with $\boldsymbol{\phi}^x_j(\boldsymbol{x}) = (\phi_j(\boldsymbol{x}), 0, 0)^T$, $\boldsymbol{\phi}^y_j(\boldsymbol{x}) = (0, \phi_j(\boldsymbol{x}), 0)^T$, and $\boldsymbol{\phi}^z_j(\boldsymbol{x}) = (0, 0, \phi_j(\boldsymbol{x}))^T$. Consequently, the solution $\boldsymbol{\rho}$ to (36) can be written as follows:

$$\boldsymbol{\rho}(\boldsymbol{x}) = \sum_{\Gamma\subset\partial K}\sum_{j\in\mathcal{J}_\Gamma} [\hat{F}^{jx}_{K|\Gamma}\boldsymbol{\rho}^{jx}_\Gamma(\boldsymbol{x}) + \hat{F}^{jy}_{K|\Gamma}\boldsymbol{\rho}^{jy}_\Gamma(\boldsymbol{x}) + \hat{F}^{jz}_{K|\Gamma}\boldsymbol{\rho}^{jz}_\Gamma(\boldsymbol{x})], \tag{38}$$

where $\boldsymbol{\rho}^{jx/y/z}_\Gamma$ is the solution, up to a rigid body motion, to the elementary problem (generalization of (21)):

$$\int_K \mathcal{K}\epsilon(\boldsymbol{\rho}^{jx/y/z}_\Gamma) : \epsilon(\boldsymbol{u}^*) = \int_\Gamma \boldsymbol{\phi}^{x/y/z}_j \cdot \boldsymbol{u}^* - \int_K (\boldsymbol{a}_1 \wedge \boldsymbol{X} + \boldsymbol{a}_2) \cdot \boldsymbol{u}^* \quad \forall \boldsymbol{u}^* \in \mathcal{U}(K) \tag{39}$$

$\boldsymbol{X}$ are barycentric coordinates in element K, and $\boldsymbol{a}_1$ and $\boldsymbol{a}_2$ are defined as follows:

$$a_1 = \frac{\int_\Gamma \boldsymbol{X} \wedge \boldsymbol{\phi}^{x/y/z}_j}{\int_K \boldsymbol{X}\cdot\boldsymbol{X}} \quad ; \quad \boldsymbol{a}_2 = \frac{1}{|K|}\int_\Gamma \boldsymbol{\phi}^{x/y/z}_j. \tag{40}$$

As for the scalar case, a PGD representation of $\boldsymbol{\rho}$ is then constructed as follows:

$$\boldsymbol{\rho}_m(\boldsymbol{x}_{ref}, \boldsymbol{p}_{geo}, \{\widehat{\boldsymbol{F}}^{jx/y/z}_{K|\Gamma}\}) = \sum_{\Gamma\subset\partial K}\sum_{j\in\mathcal{J}_\Gamma}[\hat{F}^{jx}_{K|\Gamma}\boldsymbol{\rho}^{jx}_{\Gamma,m}(\boldsymbol{x}_{ref}, \boldsymbol{p}_{geo}) + \hat{F}^{jy}_{K|\Gamma}\boldsymbol{\rho}^{jy}_{\Gamma,m}(\boldsymbol{x}_{ref}, \boldsymbol{p}_{geo}) + \hat{F}^{jz}_{K|\Gamma}\boldsymbol{\rho}^{jz}_{\Gamma,m}(\boldsymbol{x}_{ref}, \boldsymbol{p}_{geo})] \tag{41}$$

and a parameterized equilibrated stress field at the element level reads

$$\hat{\boldsymbol{\varpi}}_{h,m|K}(\boldsymbol{x}_{ref}, \boldsymbol{p}_{geo}, \{\widehat{\boldsymbol{F}}^{jx/y/z}_{K|\Gamma}\}) = \boldsymbol{\mathcal{K}}(\mathbb{J}^{-T}(\boldsymbol{p}_{geo})\underline{\nabla})^s\boldsymbol{\rho}_m(\boldsymbol{x}_{ref}, \boldsymbol{p}_{geo}, \{\widehat{\boldsymbol{F}}^{jx/y/z}_{K|\Gamma}\}). \tag{42}$$

4 | OPTIMIZATION OF TRACTIONS

The quality of the CRE estimate is related to that of constructed equilibrated tractions, so that optimizing tractions $\hat{F}_{K|\Gamma}$ is a relevant task. However, this leads to a global optimization problem that is complex to solve without sophisticated numerical methods. In previous studies,[43,54,55] a partial optimization was investigated. The basic idea was to give greater freedom in the construction of equilibrated tractions, applying the prolongation condition on nonvertex nodes alone, to improve the quality of the recovered admissible flux fields. To keep a reasonable computational cost, such an enhanced construction of equilibrated tractions may in practice be applied only in zones of high element aspect ratios or sharp gradients, in which the quality of admissible flux fields may be affected with usual procedures.

In this section, we wish to take advantage of the PGD representation (35) (which provides for a reduced model at the element level) to address a full optimization of tractions $\hat{F}_{K|\Gamma}$ by minimizing the CRE functional. This procedure, which would be out of reach with a classical approach, is highly facilitated by the explicit dependency of the admissible field $\hat{\boldsymbol{q}}_{h,m}$ on $\{\hat{F}^j_{K|\Gamma}\}$ provided by the PGD. It is referred as the HFT-PGD technique.

4.1 | Optimization problem

We define the (infinite dimensional) space of equilibrated tractions:

$$\mathcal{F} = \left\{ \{\hat{F}_\Gamma(\boldsymbol{x})\};\quad \int_K f_d + \sum_{\Gamma\subset\partial K}\int_\Gamma \eta^\Gamma_K\hat{F}_\Gamma = 0 \quad \text{for all} \quad K, \quad \eta^\Gamma_K\hat{F}_\Gamma = F_d \quad \text{if} \quad \Gamma\subset\partial_2\Omega \right\}. \tag{43}$$

In this space, we consider the (finite dimensional) subspace of tractions that have a given form on each edge/face (linear combination of shape functions):

$$\mathcal{F}_\ell = \left\{ \{\hat{F}_\Gamma(\boldsymbol{x})\}\in\mathcal{F};\quad \hat{F}_\Gamma(\boldsymbol{x}) = \sum_{j\in\mathcal{J}_\Gamma}\hat{F}^j_\Gamma\phi_j(\boldsymbol{x}) \right\} \subset \mathcal{F}. \tag{44}$$

The dimension of $\mathcal{F}_\ell$ depends on the polynomial degree of FE shape functions and the number of edges/faces. Consequently, the unknowns of the problem are interface data $\{\hat{F}^j_\Gamma\}$, which are gathered in a global vector $\widehat{\boldsymbol{F}}$ of length N_F. This way, the constraint that $\{\hat{F}^j_\Gamma\}$ provide tractions that belong to $\mathcal{F}$ can be written $\mathbb{C}\widehat{\boldsymbol{F}} = \widehat{\boldsymbol{F}}_d$.

Consequently, the optimization problem reads

$$\{\hat{F}_\Gamma(\boldsymbol{x})\}_{opt} = \underset{\{\hat{F}_\Gamma\}\in\mathcal{F}_\ell}{\arg\min}\, E^2_{CRE}\left(u_h, \hat{\boldsymbol{q}}_h(\{\hat{F}_\Gamma\})\right) \quad \text{or} \quad \widehat{\boldsymbol{F}}_{opt} = \underset{\widehat{\boldsymbol{F}},\mathbb{C}\widehat{\boldsymbol{F}}=\widehat{\boldsymbol{F}}_d}{\arg\min} E^2_{CRE}\left(u_h, \hat{\boldsymbol{q}}_h(\widehat{\boldsymbol{F}})\right). \tag{45}$$

4.2 | Solution using PGD

On the one hand, from the PGD representation (35) of $\hat{\boldsymbol{q}}_{h,m|K}$,

$$\hat{\boldsymbol{q}}_{h,m|K}(\boldsymbol{x}_{ref}, \boldsymbol{p}_{geo}, \{\hat{F}^j_\Gamma\}) = \mathbb{J}^{-T}(\boldsymbol{p}_{geo})\,\boldsymbol{\nabla}\left(\sum_{\Gamma\subset\partial K}\sum_{j\in\mathcal{J}_\Gamma}\eta^\Gamma_K\hat{F}^j_\Gamma\boldsymbol{\rho}^j_{\Gamma,m}(\boldsymbol{x}_{ref}, \boldsymbol{p}_{geo})\right), \tag{46}$$

the global admissible field $\hat{\boldsymbol{q}}_{h,m}$ computed with PGD can be written as follows:

$$\hat{\boldsymbol{q}}_{h,m} = \mathbb{N}(\boldsymbol{x}_{ref}, \boldsymbol{p}_{geo})\widehat{\boldsymbol{F}}, \tag{47}$$

where $\mathbb{N}(\boldsymbol{x}_{ref}, \boldsymbol{p}_{geo})$ is a parameterized $d \times N_F$ matrix.

On the other hand, the PGD representation of $E^2_{CRE}(u_h, \hat{\boldsymbol{q}}_{h,m}(\{\hat{F}^j_\Gamma\}))$ reads

$$\begin{aligned} E^2_{CRE}(u_h, \hat{\boldsymbol{q}}_{h,m}) &= \frac{1}{2}\int_\Omega (\hat{\boldsymbol{q}}_{h,m} - \mathcal{K}\boldsymbol{\nabla} u_h)\cdot\mathcal{K}^{-1}(\hat{\boldsymbol{q}}_{h,m} - \mathcal{K}\boldsymbol{\nabla} u_h) \\ &= \frac{1}{2}\|\hat{\boldsymbol{q}}_{h,m}\|^2_S - \int_\Omega \hat{\boldsymbol{q}}_{h,m}\boldsymbol{\nabla} u_h + \frac{1}{2}\|u_h\|^2_{\mathcal{U}} \\ &= \frac{1}{2}\widehat{\boldsymbol{F}}^T\mathbb{M}\widehat{\boldsymbol{F}} - \widehat{\boldsymbol{F}}^T\mathbb{L}\boldsymbol{U}_h + \frac{1}{2}\|u_h\|^2_{\mathcal{U}} \end{aligned} \tag{48}$$

with $\mathbb{M} = \int_\Omega \mathbb{N}^T\boldsymbol{\mathcal{K}}\mathbb{N}$ and $\mathbb{L} = \int_\Omega \mathbb{N}^T\mathbb{B}$ ($\mathbb{B}\boldsymbol{U}_h = \boldsymbol{\nabla} u_h$). Then the optimization problem is recast as follows:

$$\widehat{\boldsymbol{F}}_{opt} = \underset{\widehat{\boldsymbol{F}},\mathbb{C}\widehat{\boldsymbol{F}}=\widehat{\boldsymbol{F}}_d}{\arg\min}\left(\frac{1}{2}\widehat{\boldsymbol{F}}^T\mathbb{M}\widehat{\boldsymbol{F}} - \widehat{\boldsymbol{F}}^T\mathbb{L}\boldsymbol{U}_h\right). \tag{49}$$

It is solved using a Lagrangian functional that leads to the system:

$$\begin{pmatrix} \mathbb{M} & \mathbb{C}^T \\ \mathbb{C} & 0 \end{pmatrix}\begin{pmatrix} \widehat{\boldsymbol{F}}_{opt} \\ \Lambda \end{pmatrix} = \begin{pmatrix} \mathbb{L}\boldsymbol{U}_h \\ \widehat{\boldsymbol{F}}_d \end{pmatrix}. \tag{50}$$

We notice that elementary matrices that compose $\mathbb{M}$, $\mathbb{C}$, and $\mathbb{L}$ can be precomputed in the offline phase and defined under a PGD form with separated variables decomposition, from both matrices defined at the element level from (46) and the topology of the mesh. Technically, coefficients of elementary matrices are computed and stored once for all with a parameterized PGD form. From the topology of the mesh and the shape of elements, these coefficients are particularized by means of evaluation of PGD terms and the assembly of global matrices is performed under a sparse format without

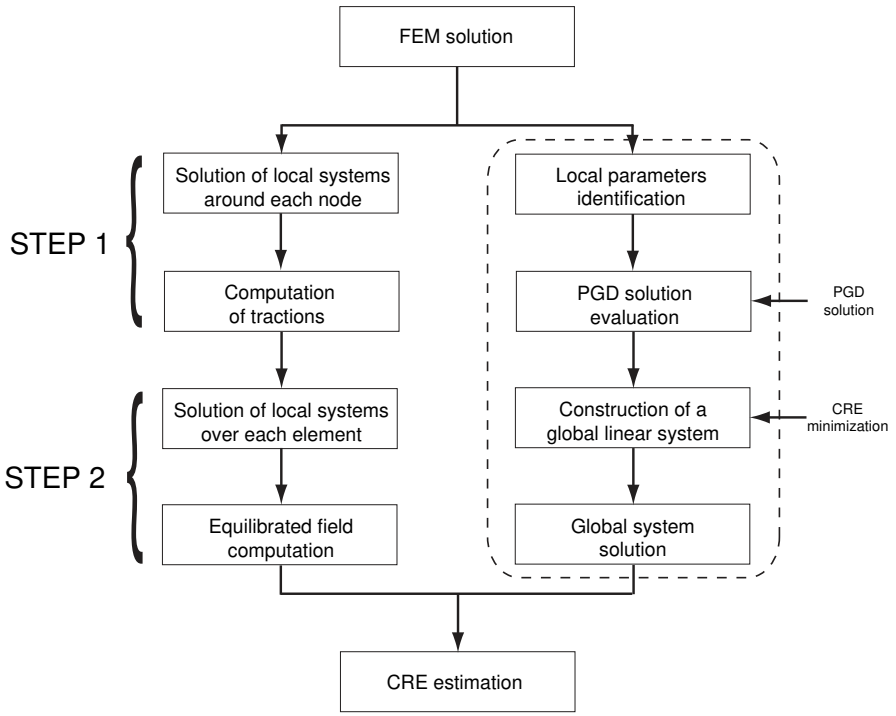

FIGURE 5 Flow chart of the classical EET approach (left) versus the HFT-PGD approach (right) to compute the CRE estimate. CRE, constitutive relation error; EET, Element Equilibration Technique; HFT, Hybrid Flux Technique; PGD, proper generalized decomposition

resorting to any numerical integration in the online phase. The global system (50) of size $(N_F+N_{F_d})\times(N_F+N_{F_d})$, N_{F_d} being the number of constraints imposed in $\mathcal{F}$, is then factorized and solved in this latter phase. The number of PGD modes that are used in this process is defined from a posteriori error estimation at the element level as suggested in Section 3.3.

Once the system (50) is inverted, the CRE estimate is directly recovered as follows:

$$E^2_{CRE} = \frac{1}{2}\widehat{\boldsymbol{F}}^T_{opt}\mathbb{M}\widehat{\boldsymbol{F}}_{opt} - \widehat{\boldsymbol{F}}^T_{opt}\mathbb{L}\boldsymbol{U}_h + \frac{1}{2}\|u_h\|^2_{\mathcal{U}^*}. \tag{51}$$

Remark 8. When considering nonlinear problems, the CRE functional may be nonlinear with respect to $\hat{\boldsymbol{q}}_{h,m}$ so that iterative minimization methods are required. An alternative is to minimize $\|\hat{\boldsymbol{q}}_{h,m} - \boldsymbol{q}_h\|_{\mathcal{S}}$.

A representation of the obtained HFT-PGD technique, that uses PGD model reduction all along the CRE process and thus leads to a convenient alternative to the classical hybrid-flux approach, is given in Figure 5.

5 | NUMERICAL RESULTS

In this section, we evaluate performance of the proposed approach on two-dimensional (2D) and three-dimensional (3D) numerical experiments. In all studied cases, we consider regular meshes such as these classically given by mesh generators (no badly shaped or distorted elements). Consequently, the geometrical parameters considered in the PGD take values that remain in a convenient interval for which PGD decompositions lead to a negligible truncation error with a reasonable number of modes. In addition, the numerical experiments involve an FE approximation with first-order Lagrange basis functions.

5.1 | 2D thermal problem over a regular physical domain

We perform discretization error estimation on a 2D holed plate Ω, which is discretized by means of a mesh composed of 3-node triangle elements (Figure 6). The plate has length $2H$ and height H with $H = 10$, and the circular hole is centered on the plate with radius $r = 1$. We consider a steady-state thermal problem and homogeneous isotropic material properties with $\mathcal{K} = \mathbb{I}$. A prescribed zero temperature is applied on the external boundary, while a normal flux $F_d = 1$ is imposed on the inner boundary, ie, on the hole boundary. Because of symmetries, only one quarter of the plate is studied.

From the associated FE solution, equilibrated tractions may be computed using the first step of the hybrid-flux (or EET) technique.

5.1.1 | Details on the PGD solution

Using notations of Figure 2, we compute parameterized solutions $\rho^j_{\Gamma^{kl},m}(\boldsymbol{x}_{ref},\alpha,\bar{x}_3,\bar{y}_3) = \alpha\sum_{i=1}^m \psi_i(\boldsymbol{x}_{ref})\delta^x_i(\bar{x}_3)\delta^y_i(\bar{y}_3)$ of (21) with a single fourth-order FE element and 20 PGD modes ($m = 20$). The domains $I_{\bar{x}_3} = [0,1]$ and $I_{\bar{y}_3} = [0.1,1]$ are discretized with 100 points each, after checking that this is sufficient to ensure an accurate description of the evolutions with respect to $\bar{x}_3$ and $\bar{y}_3$. The first 3 PGD modes of $\rho^1_{\Gamma^{12},20}$ are shown in Figure 7. In Figure 8, we represent the PGD approximation of $\rho^1_{\Gamma^{12}}$ for various configurations of parameters $\bar{x}_3$ and $\bar{y}_3$. The computation of this PGD solution is done once for all, in an offline phase and stored for later use.

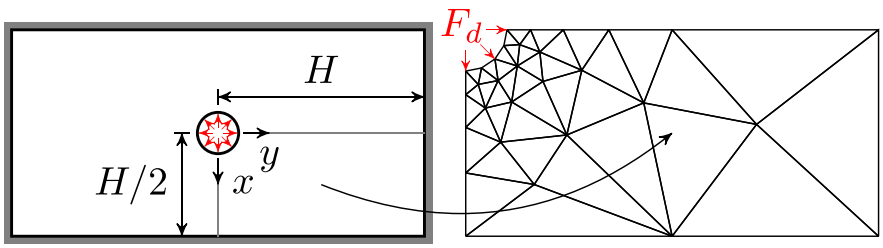

FIGURE 6 Representation of the 2D domain, associated FE mesh, and applied loading

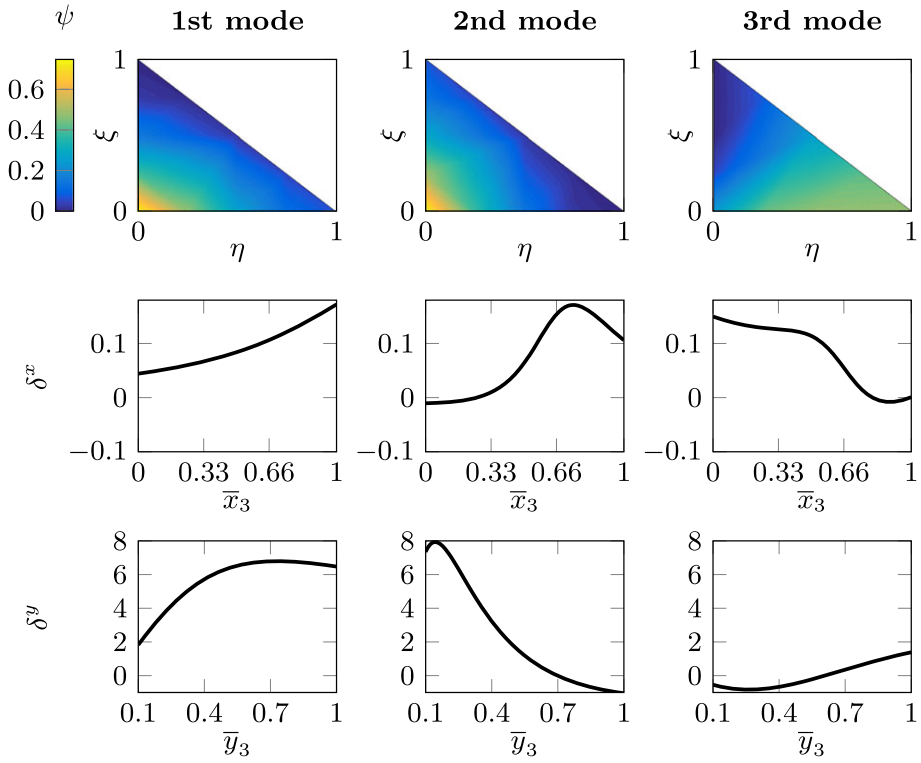

FIGURE 7 First proper generalized decomposition modes of $\rho^1_{\Gamma^{12},20}$: space functions $\psi_i(\boldsymbol{x})$ (top), and parameters functions $\delta^x_i(\bar{x}_3)$ (center) and $\delta^y_i(\bar{y}_3)$ (bottom) are represented with respect to the order i, for $i = 1, 2, 3$ (from left to right)

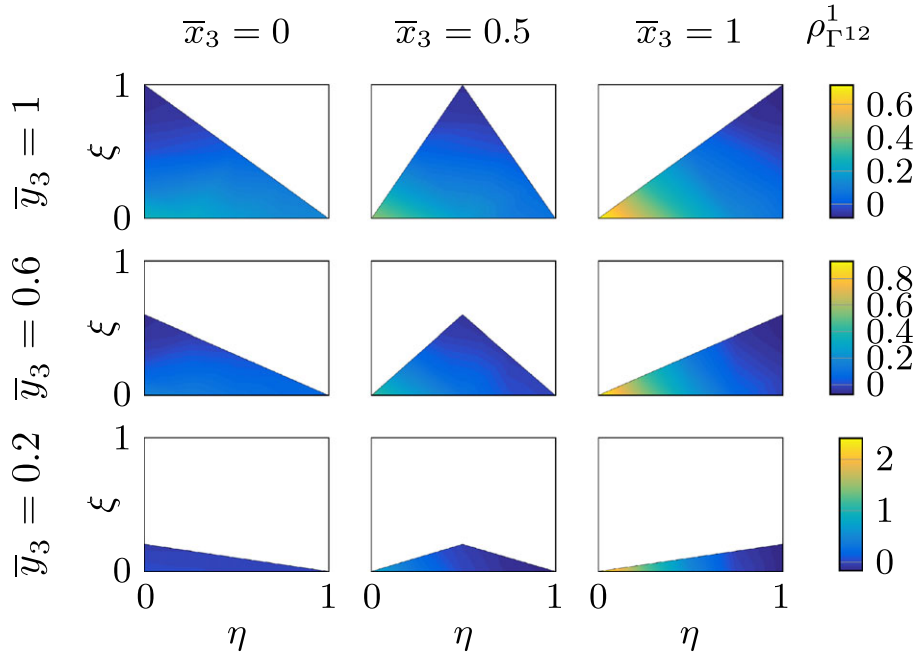

FIGURE 8 Representation of the parameterized proper generalized decomposition solution $\rho^1_{\Gamma^{12},20}$ over the element $\bar{K}$ for various parameter configurations

After identifying the PGD parameters α, $\bar{x}_3$, and $\bar{y}_3$ over each element of the mesh (see Figure 9), an accurate PGD approximation of the admissible flux $\hat{\boldsymbol{q}}_m$ can then be directly evaluated inside each element in an inexpensive online phase; we recall that this method is referred as EET-PGD method.

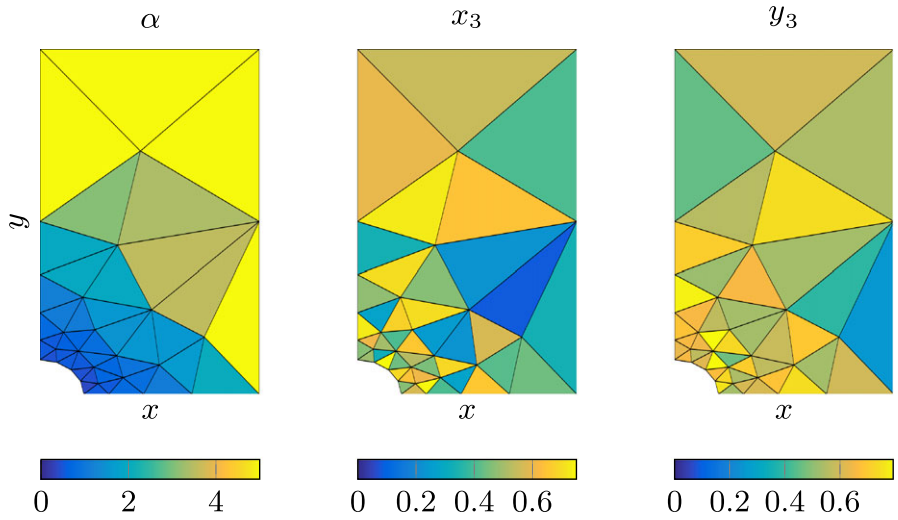

FIGURE 9 Identified values of proper generalized decomposition parameters α, $\bar{x}_3$, and $\bar{y}_3$ for each element K of the mesh

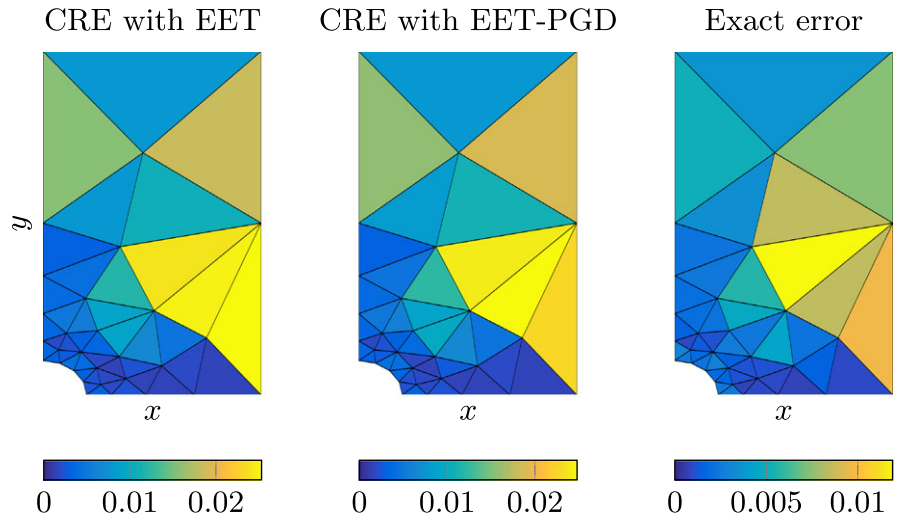

FIGURE 10 Local contributions to the constitutive relation error (CRE) estimate $2E^2_{CRE}$ obtained using either the Element Equilibration Technique (EET) technique (left) or the EET-PGD technique (center), and elementary contributions to the exact error $\|e\|^2_{\mathcal{V}}$ (right). PGD, proper generalized decomposition

5.1.2 | CRE estimate obtained from EET-PGD

From equilibrated tractions and PGD solutions, we have all ingredients to estimate the discretization error using the CRE method. In Figure 10, we compare local contributions to the CRE estimate $2E^2_{CRE}$, obtained from the EET-PGD technique when computing an admissible flux $\hat{\boldsymbol{q}}_{h,m}$, with the following: (1) contributions to the CRE estimate obtained from the classical EET technique when computing an admissible flux $\hat{\boldsymbol{q}}_h$; (2) contributions to the exact error $\|e\|^2_{\mathcal{V}}$ evaluated using a highly refined mesh (overkill solution). One observes similarities between the two CRE estimations, showing up areas where the mesh needs to be refined. These areas are correctly predicted when comparing to the exact error distribution.

Choosing $m = 20$ to compute PGD solutions in the EET-PGD technique may be unnecessary. To analyze this point, we show in Figure 11 values of the effectivity index $i_{eff} = \frac{\sqrt{2E_{CRE}}}{\|e\|_{\mathcal{V}}}$ with respect to the number m of PGD modes used to evaluate the equilibrated flux $\hat{\boldsymbol{q}}_{h,m}$. We also represent in Figure 12 the evolution of the relative error $\frac{\|\hat{\boldsymbol{q}}_{h,m}-\hat{\boldsymbol{q}}_h\|_S}{\|\hat{\boldsymbol{q}}_h\|_S}$ with respect to m, where $\hat{\boldsymbol{q}}_h$ is the equilibrated flux field constructed with the EET technique. A map of $\|\hat{\boldsymbol{q}}_{h,m} - \hat{\boldsymbol{q}}_h\|_S$ for $m = 1$, $m = 2$, and $m = 3$ is given in Figure 13. We observe that choosing $m = 7$ is enough to reconstruct an admissible flux solution, which is equivalent to the one obtained with the classical EET technique. We also observe that $m = 3$ enables to capture

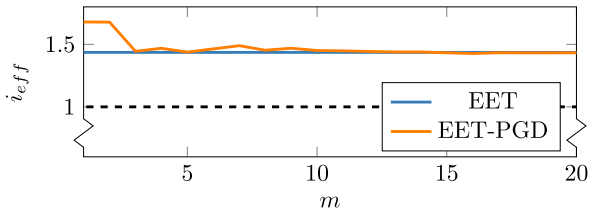

FIGURE 11 Value of the effectivity index with respect to the number of proper generalized decomposition (PGD) modes used to evaluate the equilibrated flux in the constitutive relation error estimate. EET, Element Equilibration Technique

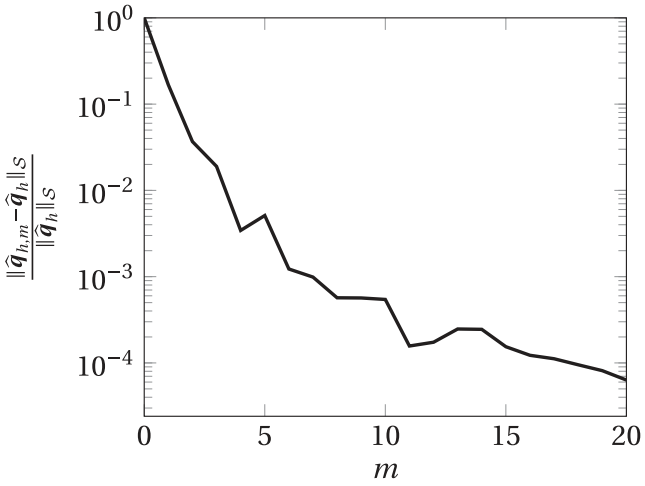

FIGURE 12 Evolution of the relative error $\|\hat{\boldsymbol{q}}_{h,m} - \hat{\boldsymbol{q}}_h\|_S / \|\hat{\boldsymbol{q}}_h\|_S$ with respect to the number of proper generalized decomposition modes used to compute $\hat{\boldsymbol{q}}_{h,m}$

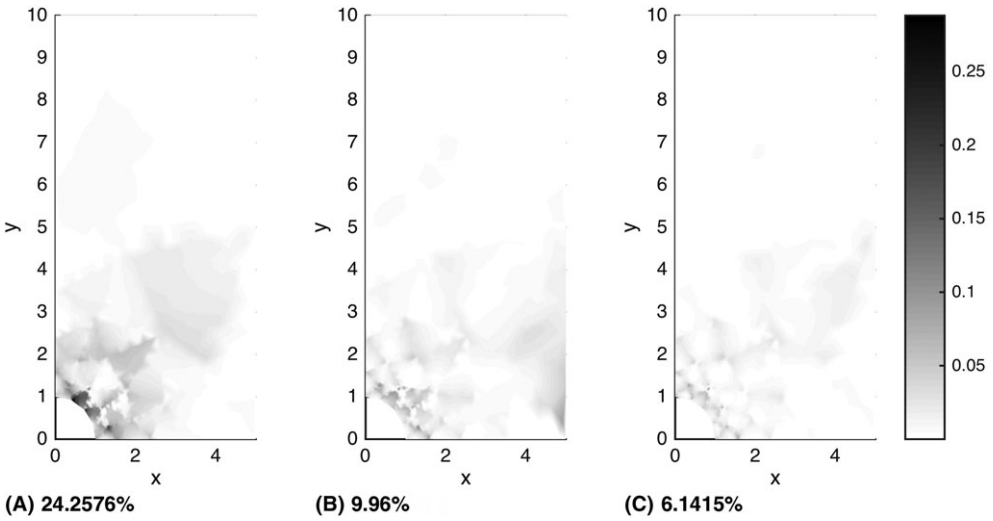

FIGURE 13 Map of the error on the flux field $\|\hat{\boldsymbol{q}}_{h,m} - \hat{\boldsymbol{q}}_h\|_S$ computed with proper generalized decomposition, for $m = 1$ (left), $m = 2$ (center), and $m = 3$ (right)

the complexity of the local problems and to provide for a relevant error estimate, even though it is not mathematically guaranteed.

5.1.3 | Speedup obtained using the PGD solution

Eventually, we compare the CPU time required to compute the equilibrated flux field depending on which method is used (see Figure 18 for a graphical representation). All the computations were performed on an Intel Core i5 2.4 GHz with

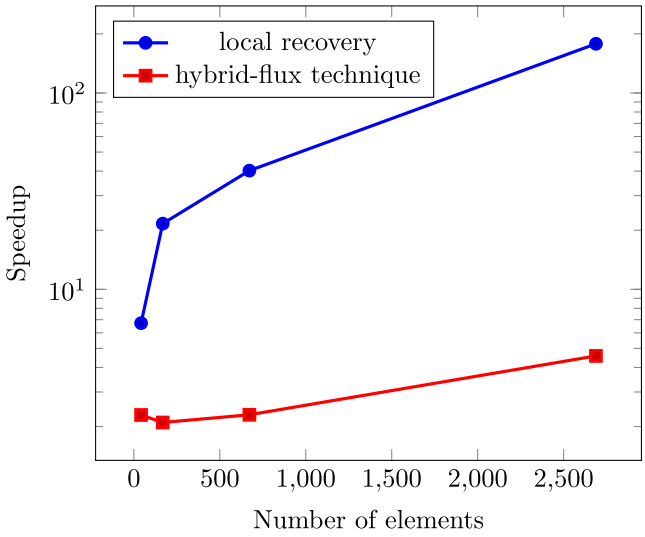

FIGURE 14 CPU speedup on the equilibrated flux step for meshes with increasing numbers of elements (speedup on the local recovery alone or on the overall hybrid-flux technique are explicited)

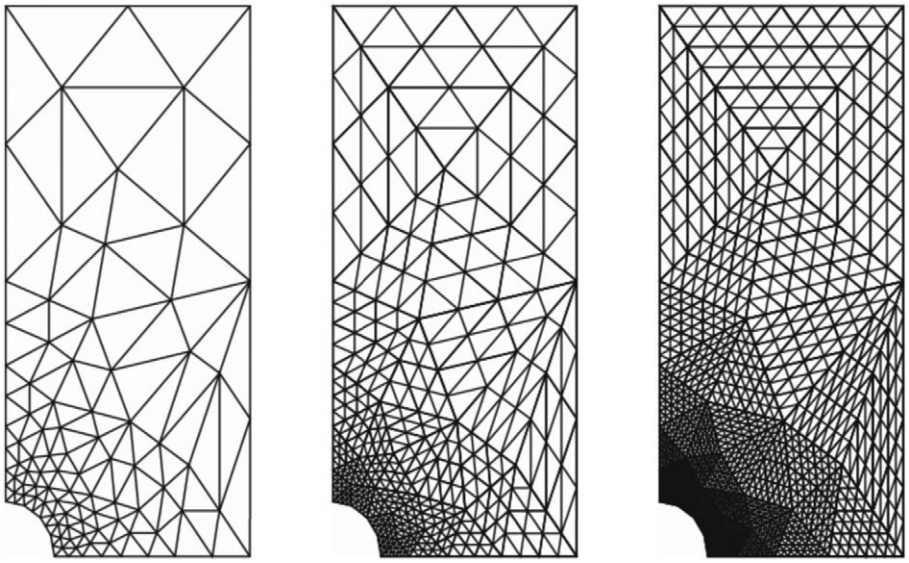

FIGURE 15 Sequence of refined meshes used to assess CPU speedup with the EET-PGD technique. EET, Element Equilibration Technique; PGD, proper generalized decomposition

8 Gb of RAM, without parallelization. Classical EET and EET-PGD techniques share as much code as possible, and only the construction and solution of the matrix problem is replaced by a simple post-processing with PGD solutions in the EET-PGD technique. Naturally, the first step with construction of equilibrated tractions is similar for both techniques.

When using the EET-PGD technique, the offline CPU cost to compute the PGD solution is 312 seconds; this solution can then be used in a multiquery context. In the online step, computing the equilibrated flux from the classical EET technique (Cholesky factorization) takes 0.01509 seconds per element (0.0587 s for the whole mesh composed of 42 elements), whereas computing the equilibrated flux from a direct evaluation of the PGD solution takes 0.00426 seconds per element (0.0077 s for the whole mesh). We thus observe a speedup of almost 10 in the second CRE step (construction of equilibrated fluxes in each element), and the global speedup on the whole hybrid-flux technique (with associated CPU cost of 0.0960 s) is about a factor 2.

In Figure 14, we represent this speedup for different levels of refinement of the initial mesh (corresponding meshes are given in Figure 15). The speedup increases as the mesh becomes finer, reaching a speedup of 125 on a 2688 elements mesh for the local recovery, while the overall hybrid-flux technique shows a speedup of magnitude 5 on this same mesh.

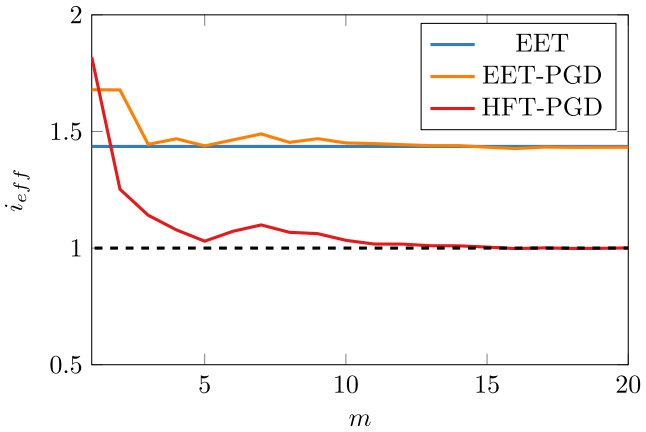

FIGURE 16 Evolution of the effectivity index with respect to the number of proper generalized decomposition (PGD) modes considered, for Element Equilibration Technique (EET), EET-PGD, and HFT-PGD. HFT, Hybrid Flux Technique

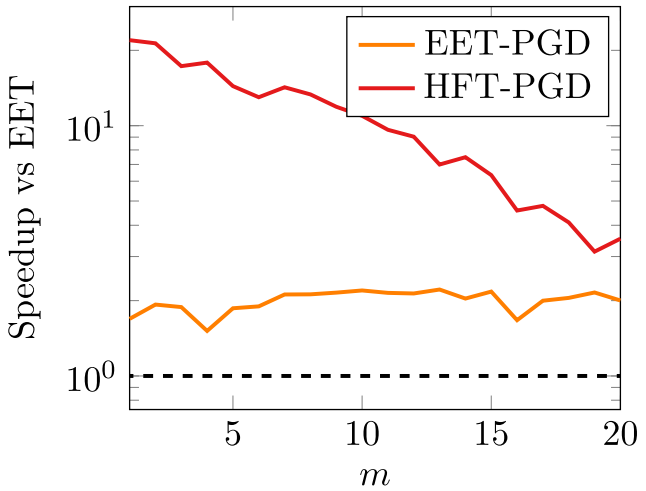

FIGURE 17 Speedup obtained for EET-PGD and HFT-PGD with respect to Element Equilibration Technique (EET), for various values of m. HFT, Hybrid Flux Technique; PGD, proper generalized decomposition

An additional step would be to reduce the CPU time of the tractions reconstruction, by optimizing implementation, to fully benefit from the use of the PGD technique; this is performed in the following section.

5.1.4 | Optimization of tractions

We now implement the HFT-PGD technique presented in Section 4, that aims at optimizing the tractions using PGD. We represent in Figure 16 the effectivity index for EET, EET-PGD, and HFT-PGD techniques, with respect to the number m of PGD modes considered. We observe that the global minimization brought by HFT-PGD largely improves the quality of the error estimate and that its tend to 1 when m increases.

In Figure 17, we give the speedup on the overall CPU cost required to compute the error estimate. We observe that HFT-PGD is particularly interesting when considering a small number of PGD modes, even though it always provides for a convenient speedup compared to EET or EET-PGD. Moreover, we observe that the speedup is stable with respect to m when considering EET-PGD alone.

In the following, we consider decompositions with 3 PGD modes. We represent in Figure 18 the normalized CPU time associated with EET, EET-PGD, and HFT-PGD methods when considering the coarsest mesh. The splitting of CPU time contributions emphasizes that the whole cost is associated with the recovery of (optimized) equilibrated tractions when using HFT-PGD.

We represent in Figure 19 the evolution of the speedup for both EET-PGD and HFT-PGD with respect to the number of elements in the mesh. We observe that there is a constant speedup of about 2 for EET-PGD compared to classical EET,

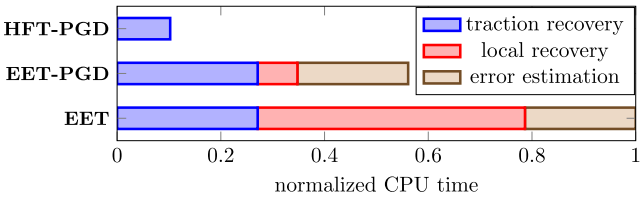

FIGURE 18 Comparison of CPU times required to compute the error estimate depending on the method which is used. EET, Element Equilibration Technique; HFT, Hybrid Flux Technique; PGD, proper generalized decomposition

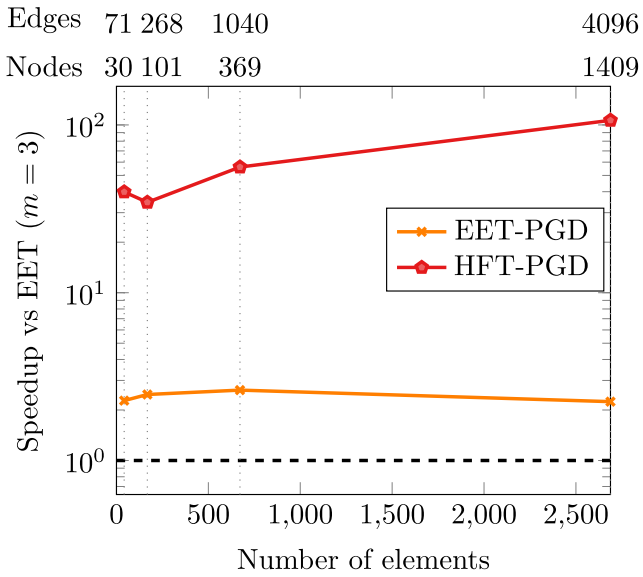

FIGURE 19 Speedup obtained for EET-PGD and HFT-PGD with respect to EET, for various mesh sizes. EET, Element Equilibration Technique; HFT, Hybrid Flux Technique; PGD, proper generalized decomposition

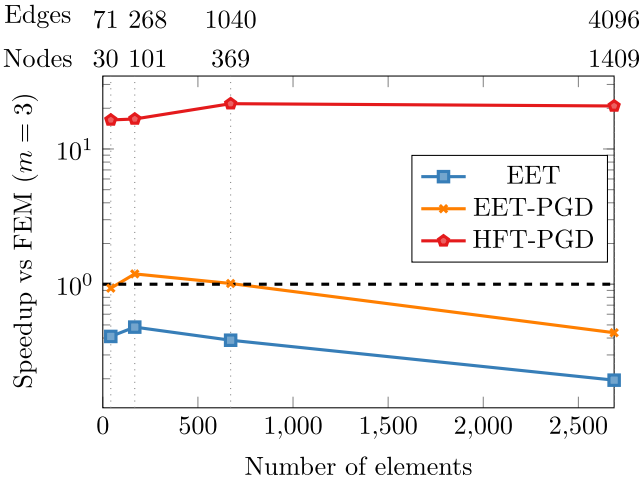

FIGURE 20 Ratio of CPU times for Element Equilibration Technique (EET), EET-PGD, and HFT-PGD with respect to the FEM CPU time, for various numbers of elements. HFT, Hybrid Flux Technique; PGD, proper generalized decomposition

and a speedup higher than 30 for HFT-PGD; this latter speedup increases with the number of elements, reaching about 100 for 2500 elements.

We eventually analyze the 3 construction techniques, ie, EET, EET-PGD, and HFT-PGD, in terms of CPU time compared to the CPU time required to perform the FEM computation (Figure 20). We observe that contrary to EET and EET-PGD, HFT-PGD leads to an error estimation procedure which is much cheaper than the FEM computation itself; even though

an additional global computation is performed in HFT-PGD, the low computational cost is due to the fact that all matrices are precomputed (no numerical integration in the online phase) and that the storage is optimized (sparse matrices are declared).

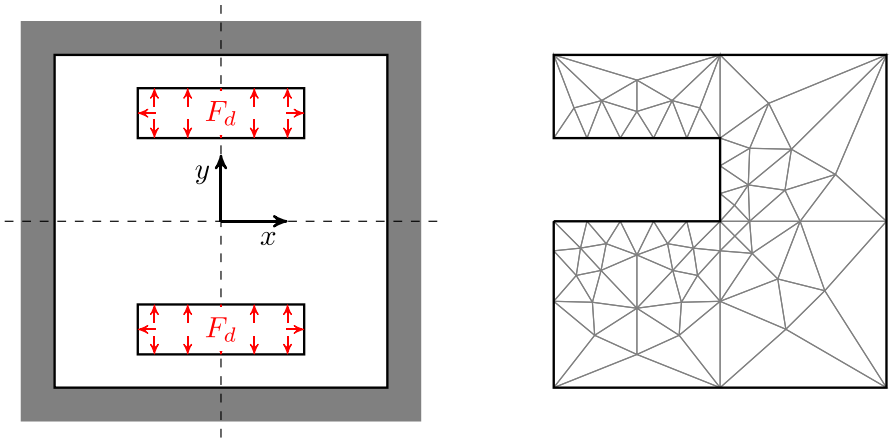

FIGURE 21 Representation of the 2D. domain, associated FE mesh, and applied loading

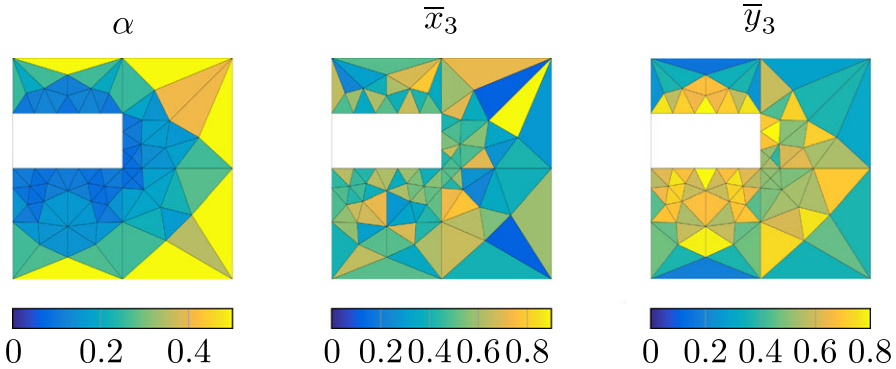

FIGURE 22 Identified values of proper generalized decomposition parameters α, $\bar{x}_3$, and $\bar{y}_3$ for each element K of the mesh

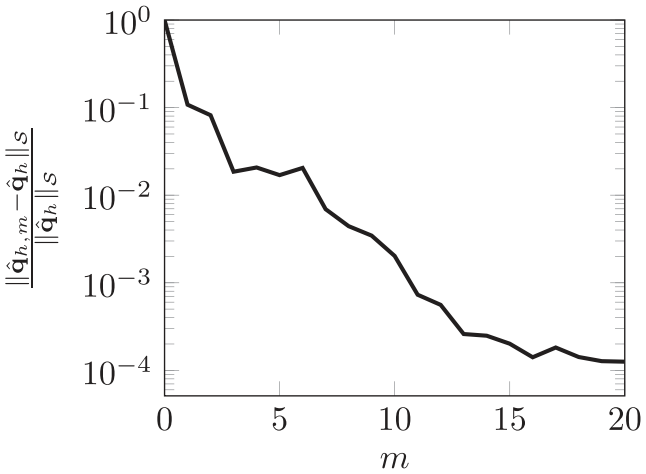

FIGURE 23 Evolution of the relative error $\|\hat{\boldsymbol{q}}_{h,m} - \hat{\boldsymbol{q}}_h\|_S / \|\hat{\boldsymbol{q}}_h\|_S$ with respect to the number of proper generalized decomposition modes used to compute $\hat{\boldsymbol{q}}_{h,m}$

5.2 | 2D thermal problem over a singular physical domain

We consider in this section the 2D squared structure represented in Figure 21, which contains two rectangular holes. The structure has size 2×2, holes have size 1×0.6, and we choose isotropic material properties with $\mathcal{K} = \mathbb{I}$. A prescribed zero

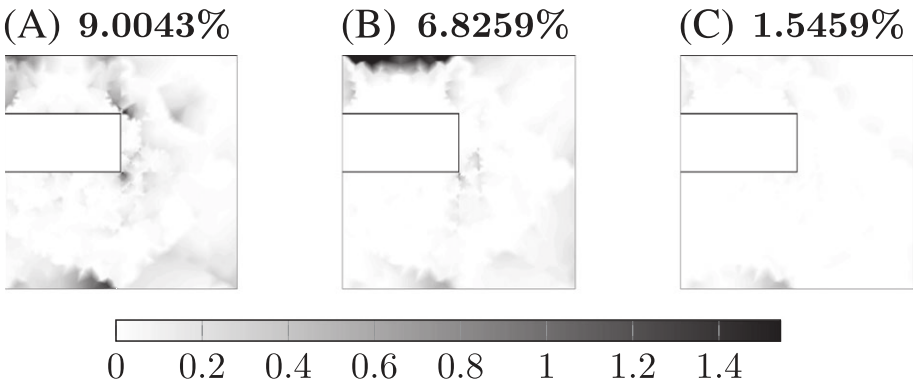

FIGURE 24 Map of the error on the flux field $\|\hat{\boldsymbol{q}}_{h,m} - \hat{\boldsymbol{q}}_h\|_S$ computed with proper generalized decomposition, for $m = 1$ (left), $m = 2$ (center), and $m = 3$ (right)

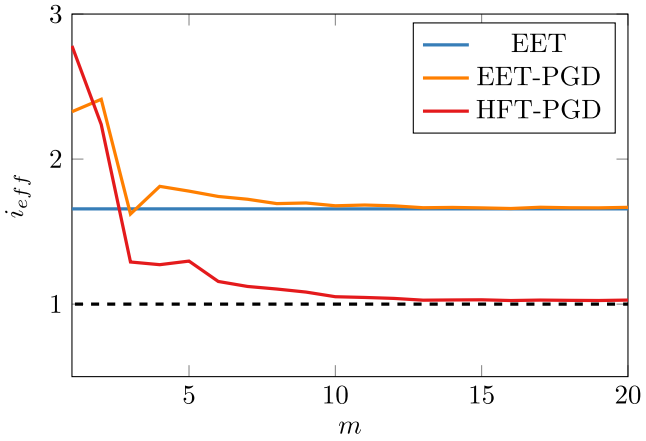

FIGURE 25 Value of the effectivity index with respect to the number of proper generalized decomposition (PGD) modes used to evaluate the equilibrated flux in the constitutive relation error estimate. EET, Element Equilibration Technique; HFT, Hybrid Flux Technique

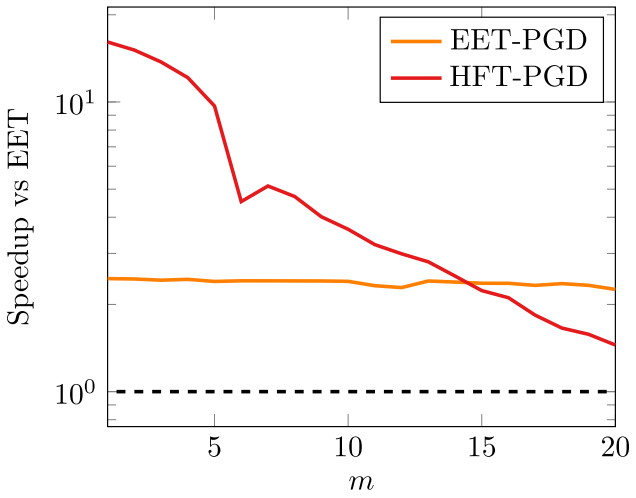

FIGURE 26 Speedup obtained for EET-PGD and HFT-PGD with respect to Element Equilibration Technique (EET), for various values of m. HFT, Hybrid Flux Technique; PGD, proper generalized decomposition

temperature is applied on the external boundary, while a normal flux $F_d = -1$ is applied on hole boundaries. Exploiting symmetries, one quarter of the structure is studied.

5.2.1 | Computation of admissible fluxes using PGD

The FE mesh that is used being made of 3-node triangle elements, PGD solutions associated to an element are the same as in Section 5.1. The values of PGD parameters α, $\bar{x}_3$, and $\bar{y}_3$ over each element of the mesh are given in Figure 22.

Considering the EET-PGD, ie, using PGD for given tractions obtained from classical equilibration techniques, we represent in Figure 23 the evolution of the relative error $\frac{\|\hat{\boldsymbol{q}}_{h,m}-\hat{\boldsymbol{q}}_h\|_S}{\|\hat{\boldsymbol{q}}_h\|_S}$ with respect to m, where $\hat{\boldsymbol{q}}_h$ is the equilibrated flux field constructed with the EET technique. A map of $\|\hat{\boldsymbol{q}}_{h,m} - \hat{\boldsymbol{q}}_h\|_S$ for $m = 1$, $m = 2$, and $m = 3$ is also given in Figure 24. We

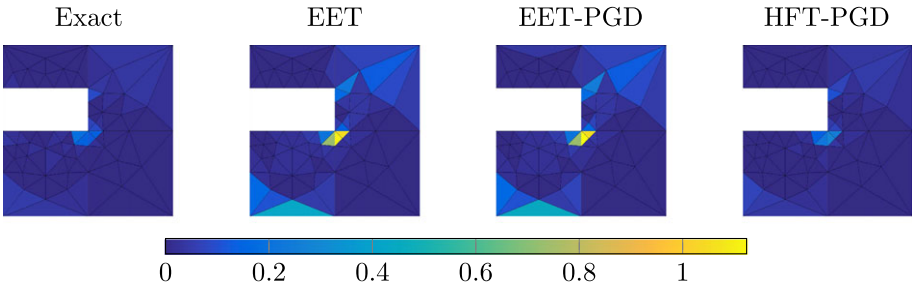

FIGURE 27 Local contributions to the exact error $\|e\|^2_{U'}$ and to the constitutive relation error estimate $2E^2_{CRE}$ obtained using Element Equilibration Technique (EET), EET-PGD, or HFT-PGD techniques (from left to right). HFT, Hybrid Flux Technique; PGD, proper generalized decomposition

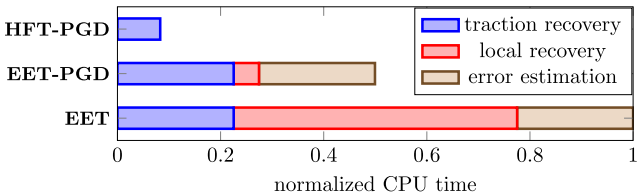

FIGURE 28 Comparison of CPU times required to compute the error estimate depending on the method which is used. EET, Element Equilibration Technique; HFT, Hybrid Flux Technique; PGD, proper generalized decomposition

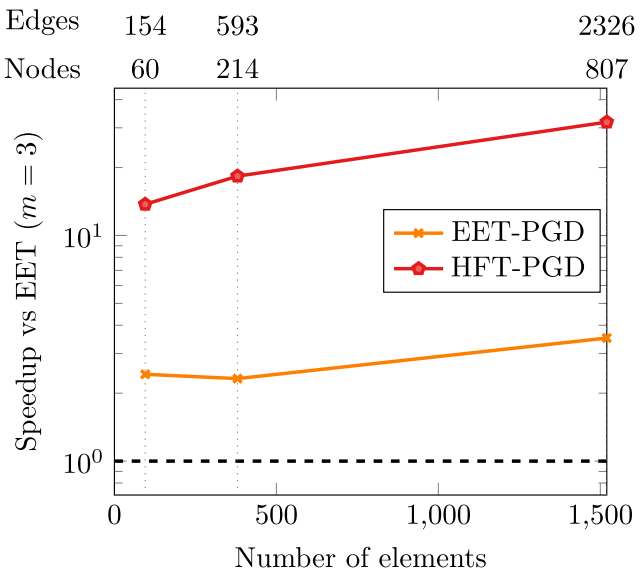

FIGURE 29 Speedup obtained for EET-PGD and HFT-PGD with respect to Element Equilibration Technique (EET), for various mesh sizes. HFT, Hybrid Flux Technique; PGD, proper generalized decomposition

still observe that a small number of PGD modes is necessary to reconstruct an admissible flux solution, which is equivalent to the one obtained with the classical EET technique ($m = 3$ already enables to capture the complexity of the local problems).

5.2.2 | Comparison between EET, EET-PGD, and HFT-PGD

We represent in Figure 25 the effectivity index when computing the CRE error estimate with EET, EET-PGD, or HFT-PGD techniques, with respect to the number m of PGD modes. We still observe that HFT-PGD enables to get an effectivity index close to 1 for $m \geq 3$. We give in Figure 26 the speedup obtained using EET-PGD or HFT-PGD on the overall CPU time required to compute the error estimate. In the range of values of m that we consider ($m \leq 10$), EET-PGD and HFT-PGD are cheaper than EET while HFT-PGD is cheaper than EET-PGD.

In the following, we consider decompositions with 3 PGD modes. We compare in Figure 27 the elementary contributions to the CRE estimate $2E^2_{CRE}$ (obtained from EET, EET-PGD, or HFT-PGD techniques) with contributions to the exact error

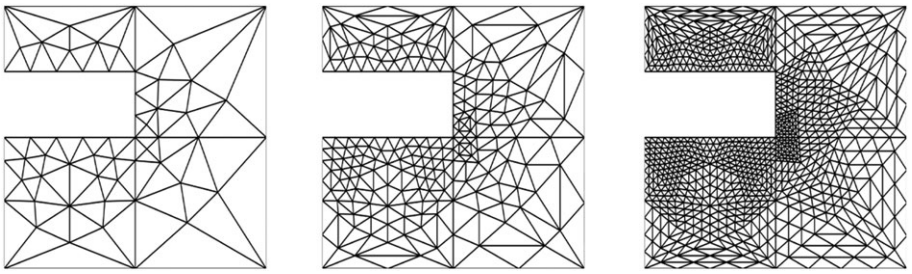

FIGURE 30 Sequence of refined meshes used to assess CPU speedup

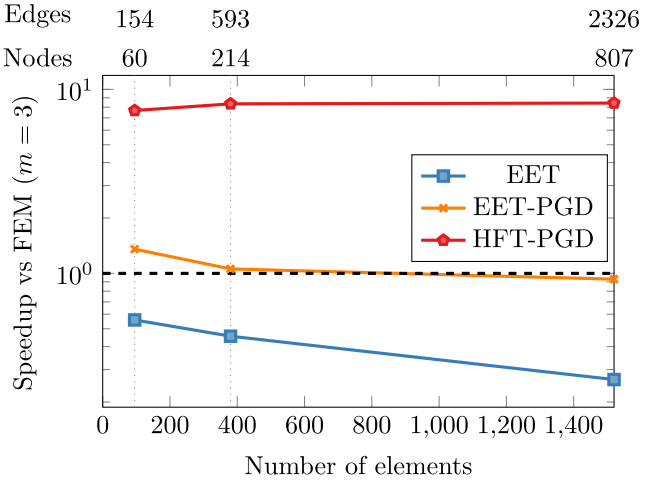

FIGURE 31 Ratio of CPU times for Element Equilibration Technique (EET), EET-PGD, and HFT-PGD with respect to the FEM CPU time, for various numbers of elements. HFT, Hybrid Flux Technique; PGD, proper generalized decomposition

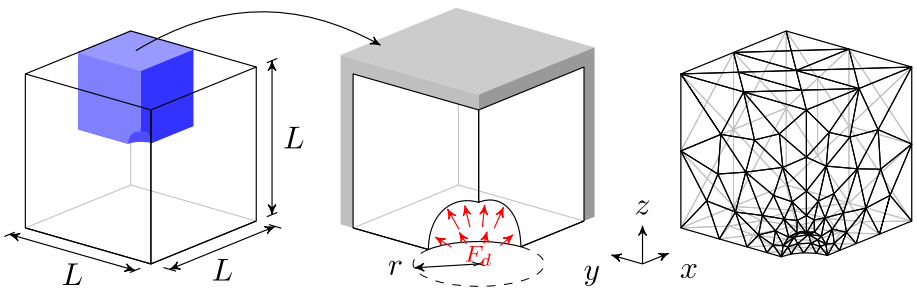

FIGURE 32 Representation of the 3D domain, associated FE mesh, and applied loading

$\|e\|^2_{\mathcal{V}}$ (evaluated from an overkill solution). We observe that error representations are similar between EET and EET-PGD, and the one given by HFT-PGD is very close to the exact one.

We represent in Figure 28 the normalized CPU time associated with EET, EET-PGD, and HFT-PGD techniques. The associated speedup provided by EET-PGD and HFT-PGD compared to EET is shown in Figure 29; it is given with respect to the mesh size by considering different levels of refinement of the initial mesh (see Figure 30). We observe that there is a constant speedup of about 2 to 3 for EET-PGD compared to classical EET, and a speedup higher than 10 for HFT-PGD; this

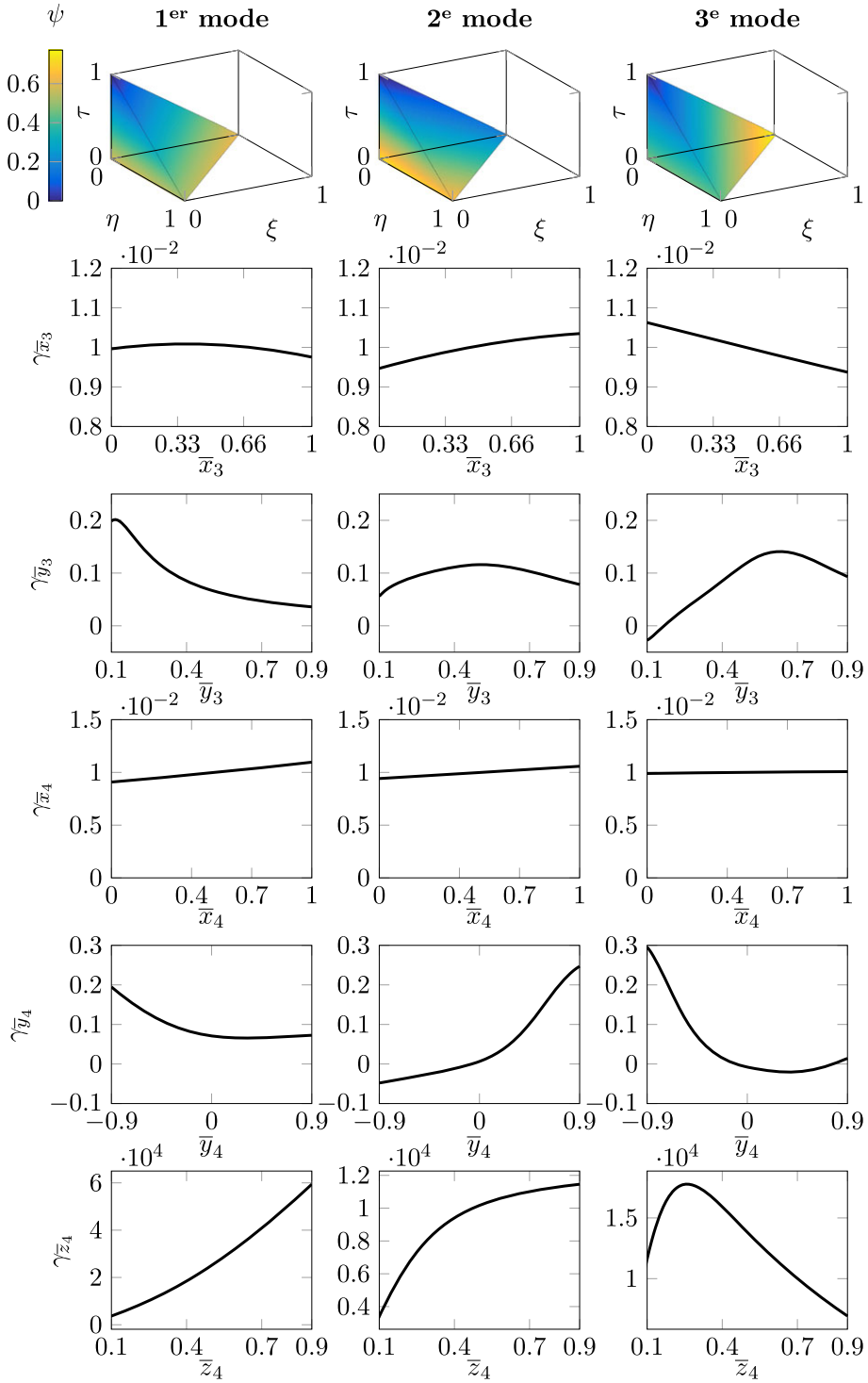

FIGURE 33 First 3 proper generalized decomposition modes (from left to right) of $\rho^1_{\Gamma^{124},20}$ with from top to bottom: space functions $\psi_i(\boldsymbol{x})$, and parameters functions $\delta_i^{x_3}(\bar{x}_3)$, $\delta_i^{y_3}(\bar{y}_3)$, $\delta_i^{x_4}(\bar{x}_4)$, $\delta_i^{y_4}(\bar{y}_4)$, and $\delta_i^{z_4}(\bar{z}_4)$

latter speedup increases with the number of elements, reaching about 30 for 1500 elements. Eventually, when analyzing performance of EET, EET-PGD, and HFT-PGD in terms of CPU time compared to the CPU time required to perform the FEM computation (Figure 31), we observe EET-PGD has a CPU cost comparable to the initial FEM computation whereas HFT-PGD leads to an error estimation procedure which is much cheaper than the initial FEM computation (speedup of about 8).

5.3 | 3D thermal problem

We now consider discretization error estimation on a 3D holed cubical domain Ω, according to a given mesh composed of 4-node tetrahedron elements (Figure 32). The cube has edge length $L = 1$, and a spherical hole is centered on the cube with radius $r = 0.2$. We consider a steady-state thermal problem and homogeneous isotropic material properties with $\mathcal{K} = \mathbb{I}$. A prescribed zero temperature is applied on the external boundary, while a flux $F_d = 1$ is imposed on the inner boundary, ie, on the hole boundary. Owing to problem symmetries, only one-eighth of the structure is studied.

From the associated FE solution, equilibrated tractions may be computed using the first step of the hybrid-flux (or EET) technique.

5.3.1 | Details on the PGD solution

Using notations of Figure 3, we compute parameterized solutions $\rho^{j}_{\Gamma^{klt},m}(\boldsymbol{x}_{ref}, \alpha, \bar{x}_3, \bar{y}_3, \bar{x}_4, \bar{y}_4, \bar{z}_4)$ of (21) with a single fourth-order FE element and 20 PGD modes ($m = 20$). The domains associated with each geometrical parameter are discretized with 100 points each, after checking that this is sufficient to ensure an accurate description of the evolutions with respect to these parameters. Furthermore, a high-order SVD (HOSVD) technique is applied to the Jacobian terms appearing in (26) to recover an affine dependency with respect to the parameters (about 1000 modes are kept). The first 3 PGD modes of $\rho^{1}_{\Gamma^{124},20}$ are shown in Figure 33. The computation of this PGD solution is done once for all, in an offline phase and stored for later use.

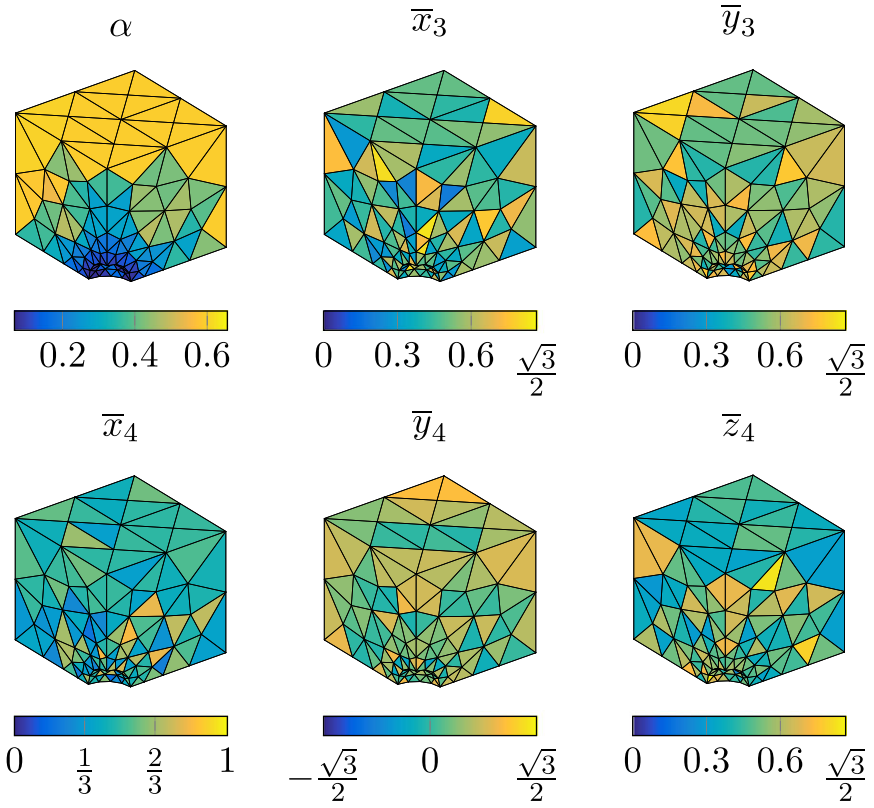

FIGURE 34 Identified values of proper generalized decomposition parameters $\alpha, \bar{x}_3, \bar{y}_3, \bar{x}_4, \bar{y}_4$, and $\bar{z}_4$ for each element K of the mesh

5.3.2 | Performance of HFT-PGD

After identifying the PGD parameters over each element of the mesh (see Figure 34), an accurate PGD approximation of the admissible flux $\hat{\boldsymbol{q}}_m$ can then be directly evaluated inside each element in an inexpensive online phase.

In Figure 35, we compare local contributions to the CRE estimate $2E^2_{CRE}$ obtained from the HFT-PGD technique (with $m = 20$) with those obtained from the classical EET technique. The estimate value is 2.83 and the CPU time is 624 seconds when using the EET technique, whereas the estimate value is 2.67 and the CPU time is 219 seconds when using the HFT-PGD technique (speedup of 2.8 and sharper estimate).

We give in Figure 36 the evolution of the value of the error estimate obtained using the HFT-PGD technique (compared to the classical EET technique) with respect to the number m of PGD modes used. We observe that a relevant error estimate is obtained with HFT-PGD for $m \geq 8$ and that a sharp error estimate can be recovered considering $m \geq 16$. The speedup provided by HFT-PGD compared to EET is shown in Figure 37; it is given with respect to the mesh size by considering different levels of refinement of the initial mesh, and for different values of m. We observe here that HFT-PGD remains competitive compared to classical EET while $m \leq 10$. In addition, comparing CPU time with that of the initial FEM computation (Figure 38) confirms that performance of HFT-PGD in terms of computational cost for this 3D case is affected when choosing $m \geq 10$. This may be practically changed by using a better implementation and storage of PGD representations.

5.4 | 3D elastoplasticity problem

As a last numerical experiment, we consider error estimation on 3D structure made of a elastoplastic material (Ludwik law) and according to a mesh composed of 8-node hexahedron elements (see Figure 39), as described in Hild et al.[56] It corresponds to the numerical simulation of a tensile test on a nodular graphite cast iron sample. The structure is clamped on its bottom side and submitted on its top side to a given displacement field obtained from a linear interpolation of experimentally imposed boundary conditions (see Hild et al[56]). The other sides are free.

The initial mesh is made of $3 \times 5 \times 10$ H8-elements (mesh 1), but refinements with $6 \times 10 \times 20$ elements (mesh 2), $9 \times 15 \times 30$ elements (mesh 3), and $12 \times 20 \times 40$ elements (mesh 4) are also considered. The external loading is applied by means of 10 steps in the nonlinear iterative algorithm. Using the concept of dissipation error introduced in Section 2.2.3,

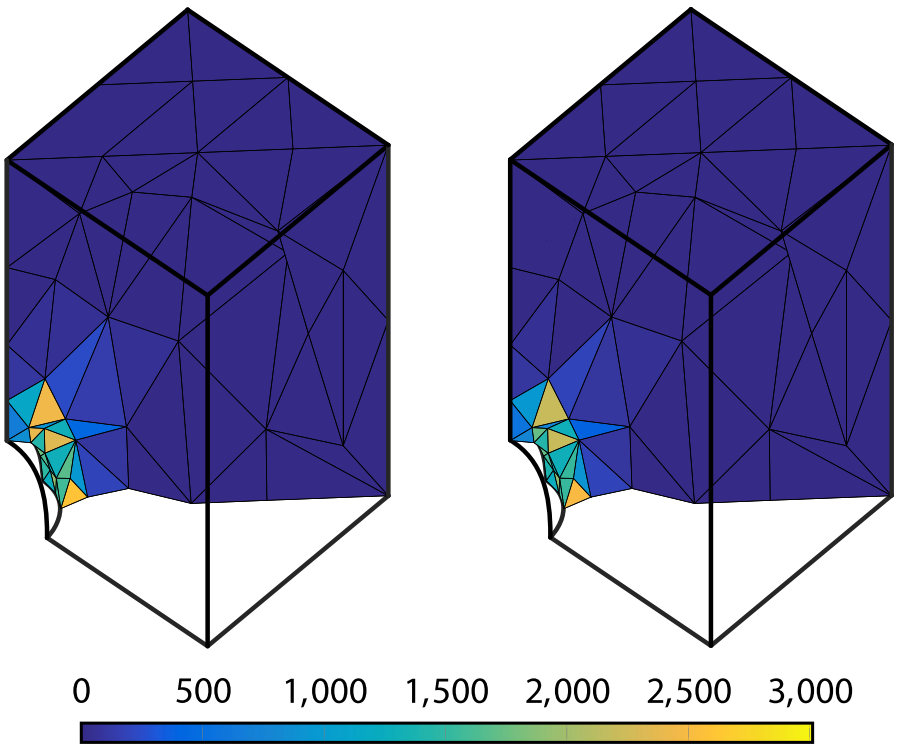

FIGURE 35 Local contributions to the constitutive relation error estimate $2E^2_{CRE}$ obtained using either the Element Equilibration Technique technique (left) or the HFT-PGD technique (right). HFT, Hybrid Flux Technique; PGD, proper generalized decomposition

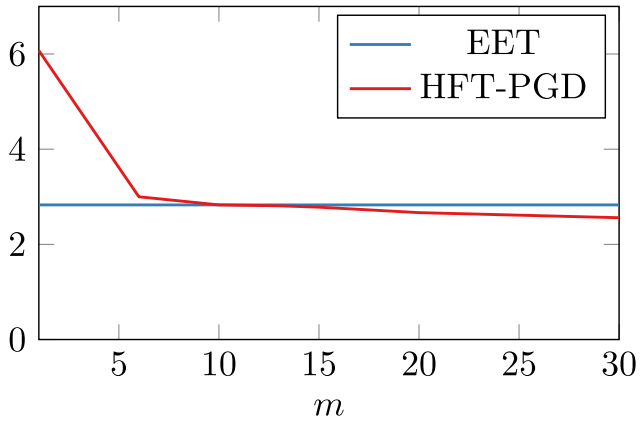

FIGURE 36 Evolutions of the error estimates obtained with Element Equilibration Technique (EET) and HFT-PGD techniques with respect to m. HFT, Hybrid Flux Technique; PGD, proper generalized decomposition

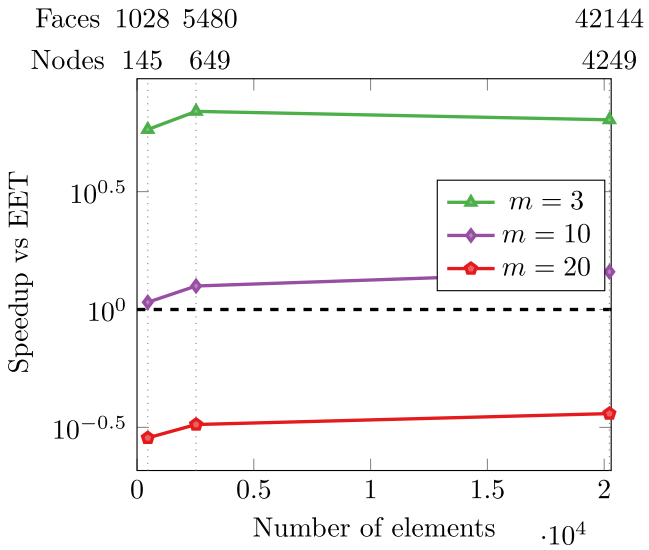

FIGURE 37 Speedup obtained for HFT-PGD with respect to Element Equilibration Technique (EET), for various mesh sizes and different values of m. HFT, Hybrid Flux Technique; PGD, proper generalized decomposition

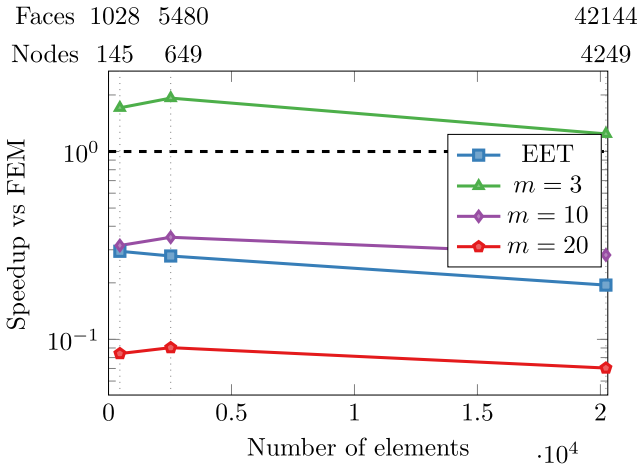

FIGURE 38 Ratio of CPU times for Element Equilibration Technique (EET), EET-PGD, and HFT-PGD with respect to the FEM CPU time, for various numbers of elements. HFT, Hybrid Flux Technique; PGD, proper generalized decomposition

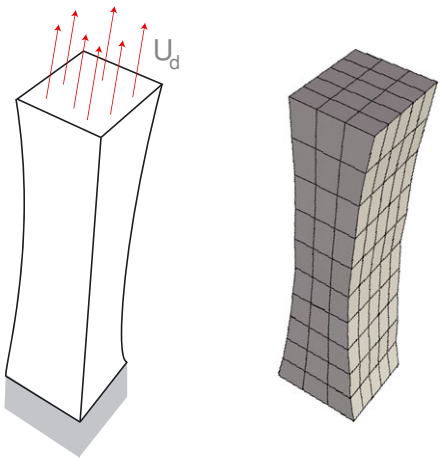

FIGURE 39 Representation of the 3D domain with associated FE mesh

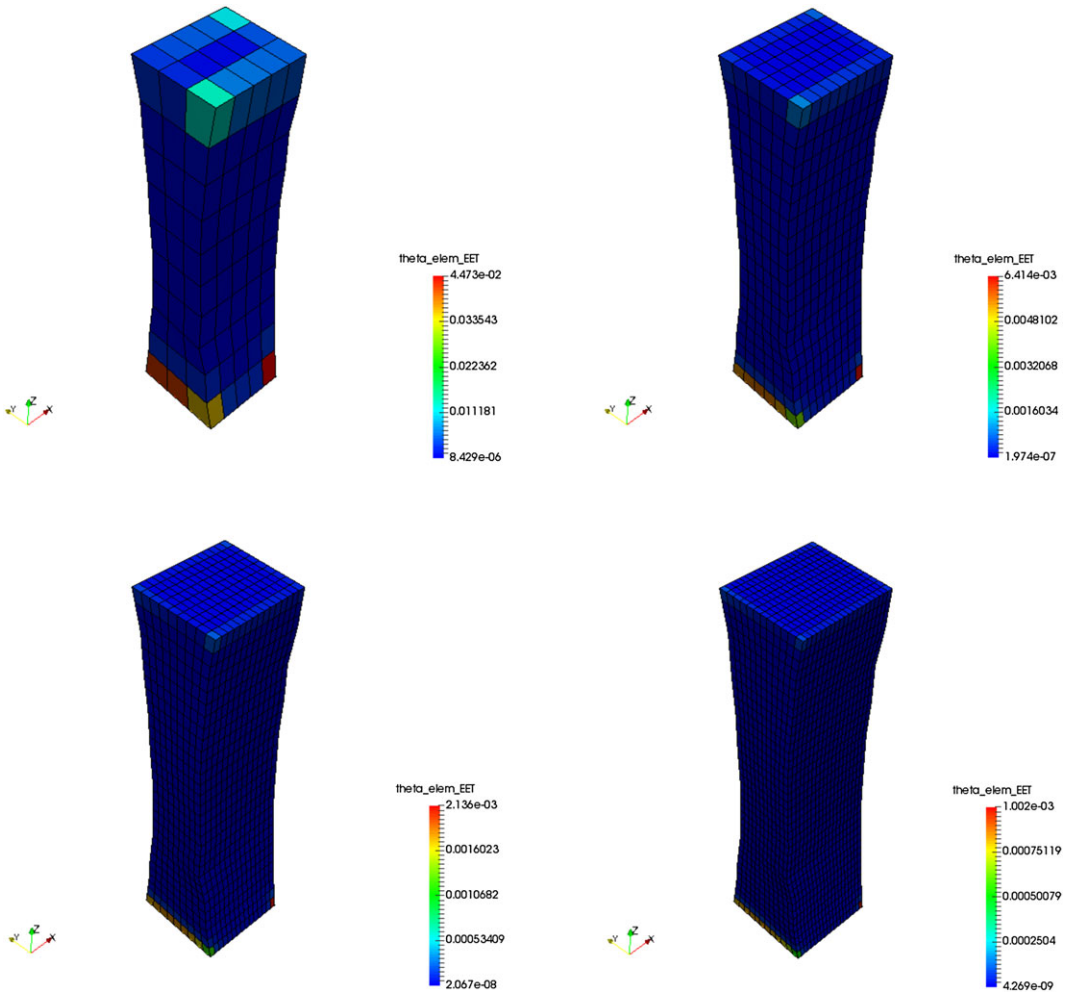

FIGURE 40 Local contributions to the CRE estimate $2E^2_{CRE}$ obtained using the Element Equilibration Technique (EET) technique associated with meshes 1, 2, 3, and 4 (from left to right)

as well as the classical EET technique to construct an admissible stress field $\hat{\boldsymbol{\sigma}}_h$ at each time point, the CRE error estimate $2E^2_{CRE}$ can be obtained. Local contributions to this estimate are shown in Figure 40.

We now assess performance of EET-PGD and HFT-PGD on this specific application. Because of the regular meshes that are used, PGD parameter values remain in a limited interval so that very few PGD modes are required to obtain an

TABLE 1 Performance of EET-PGD and HFT-PGD in terms of effectivity index and speedup compared to classical EET

	Effectivity index EET	Effectivity index EET-PGD	Speedup EET-PGD vs EET	Effectivity index HFT-PGD	Speedup HFT-PGD vs EET
Mesh 1	1.36	1.37	20.49	1.09	31.45
Mesh 2	1.33	1.35	28.72	1.11	39.09
Mesh 3	1.30	1.31	32.44	1.08	43.13
Mesh 4	1.37	1.37	36.18	1.06	48.24

Abbreviations: EET, Element Equilibration Technique; HFT, Hybrid Flux Technique; PGD, proper generalized decomposition.

accurate solution over each element. We choose $m = 5$ in practice, and we report in Table 1 the performance of EET-PGD and HFT-PGD in terms of effectivity index and speedup compared to classical EET, for the 4 meshes described previously. We observe large speedups for both methods, due to the fact that a limited number of PGD modes is considered and that the equilibration procedure has to be performed at each iteration step.

6 | CONCLUSIONS AND PROSPECTS

We presented a general framework that highlights the original and beneficial use of PGD in verification procedures performed by means of the CRE concept. Based on an offline/online strategy, this framework involves PGD representations at the level of each element of the finite element mesh. This drastically decreases the computational cost and technicalities that are essentially associated with the computation of admissible fields. It thus facilitates practical implementation, decreases CPU time, and increases the quality of the CRE error estimate.

As the proposed technique is focused on balance equations alone, it directly extends to any nonlinear time-dependent mechanical problem. In this framework, we forecast a large speedup in industrial applications due to the fact that the construction of admissible fields needs to be performed at each time step and that the speedup increases with the number of elements. We thus believe this work paves the way to robust, practical, and real-time methods for controlling FEM simulations performed by Computational Mechanics software.

Additional studies on the proposed technique could be investigated: (1) application to higher-order elements on complex meshes; (2) consideration as a tool for designing optimal meshes, as well as for mesh refinement on the fly; and (3) comparison with concurrent approaches that exhibit an offline stage such as the patch-based mixed finite element approach.[24,29] All these points will be the topics of forthcoming research works.

ORCID

Ludovic Chamoin http://orcid.org/0000-0002-8361-0757

REFERENCES

1. Verfürth R. *A Review of a Posteriori Error Estimation and Adaptive Mesh Refinement Techniques*. Stuttgart: Wiley-Teubner; 1996.
2. Babuška I, Strouboulis T. *The Finite Element Method and Its Reliability*. Oxford: Oxford University Press; 1999.
3. Ladevèze P, Pelle JP. *Mastering Calculations in Linear and Nonlinear Mechanics*. New York: Springer NY; 2004.
4. Chamoin L, Díez P (ed). *Verifying Calculations, Forty Years On: An Overview of Classical Verification Techniques for FEM Simulations*. Springer International Publishing; 2015.
5. Zienkiewicz O, Zhu J. A simple error estimator and adaptive procedure for practical engineering analysis. *Int J Numer Meth Eng*. 1987;24:337-357.
6. Babuška I, Rheinboldt WC. A posteriori error estimates for the finite element method. *Int J Numer Meth Eng*. 1978;12:1597.
7. Ladevèze P, Leguillon D. Error estimate procedure in the finite element method and application. *SIAM J Numer Anal*. 1983;20(3):485-509.
8. Comparaison LP. *De Modèles De Milieux Continus*, Thèse d'état. Paris: Université P. et M. Curie; 1975.
9. Destuynder P, Métivet B. Explicit error bounds in a conforming finite element method. *Math Comput*. 1999;68(288):1379-1396.
10. Ladevèze P, Moës N. A new a posteriori error estimation for nonlinear time-dependent finite element analysis. *Comput Meth Appl Mechanics Eng*. 1998;157:45-68.
11. Ladevèze P. Constitutive relation error estimations for finite element analyses considering (visco)-plasticity and damage. *Int J Numer Meth Eng*. 2001;52(5-6):527-542.

12. Ladevèze P. Strict upper error bounds for calculated outputs of interest in computational structural mechanics. *Comput Mechanics*. 2008;42(2):271-286.
13. Ladevèze P, Chamoin L. Calculation of strict error bounds for finite element approximations of nonlinear pointwise quantities of interest. *Int J Numer Meth Eng*. 2010;84:1638-1664.
14. Ladevèze P, Pled F, Chamoin L. New bounding techniques for goal-oriented error estimation applied to linear problems. *Int J Numer Meth Eng*. 2013;93(13):1345-1380.
15. Wang L, Chamoin L, Ladevèze P, Hongzhi Z. Computable upper and lower bounds on eigenfrequencies. *Comput Meth Appl Mechanics Eng*. 2016;302:27-43.
16. Ladevèze P, Chamoin L. *The Constitutive Relation Error Method: A General Verification Tool. Verifying Calculations, Forty Years on: an Overview of Classical Verification Techniques for FEM Simulations*. Springer International Publishing; 2015.
17. Ladevèze P, Maunder EAW. A general method for recovering equilibrating element tractions. *Comput Meth Appl Mechanics Eng*. 1996;137:111-151.
18. Carstensen C, Funken SA. Fully reliable localized error control in the FEM. *SIAM J Sci Comput*. 2000;21(4):1465-1484.
19. Machiels L, Maday Y, Patera A. A flux-free nodal Neumann subproblem approach to output bounds for partial differential equations. *Comptes Rendus Académie des Sciences - Mcanique, Paris*. 2000;330(1):249-254.
20. Cottereau R, Díez P, Huerta A. Strict error bounds for linear solid mechanics problems using a subdomain based flux-free method. *Comput Mechanics*. 2009;44(4):533-547.
21. Gallimard L. A constitutive relation error estimator based on traction-free recovery of the equilibrated stress. *Int J Numer Meth Eng*. 2009;78(4):460-482.
22. Moitinho de Almeida JP, Maunder EAW. Recovery of equilibrium on star patches using a partition of unity technique. *Int J Numer Meth Eng*. 2009;79:1493-1516.
23. Parès N, Santos H, Díez P. Guaranteed energy error bounds for the Poisson equation using a flux-free approach: solving the local problems in subdomains. *Int J Numer Meth Eng*. 2009;79:1203-1244.
24. Braess D, Pillwein V, Schöberl J. Equilibrated residual error estimates are *p*-robust. *Comput Meth Appl Mechanics Eng*. 2009;198:1189-1197.
25. Ern A, Vohralik M. A posteriori error estimation based on potential and flux reconstruction for the heat equation. *SIAM J Numer Anal*. 2010;345(48):198-223.
26. Ladevèze P, Chamoin L, Florentin E. A new non-intrusive technique for the construction of admissible stress fields in model verification. *Comput Meth Appl Mechanics Eng*. 2010;199(9-12):766-777.
27. Pled F, Chamoin L, Ladevèze P. On the techniques for constructing admissible stress fields in model verification: performances on engineering examples. *Int J Numer Meth Eng*. 2011;88(5):409-441.
28. Rey V, Gosselet P, Rey C. Study of the strong prolongation equation for the construction of statically admissible stress fields: implementation and optimization. *Comput Meth Appl Mechanics Eng*. 2014;268:82-104.
29. Ern A, Vohralik M. Polynomial-degree-robust a posteriori estimates in a unified setting for conforming, nonconforming, discontinuous Galerkin, and mixed discretizations. *SIAM J Numer Anal*. 2015;53(2):1058-1081.
30. Chinesta F, Ammar A, Cueto E. Recent advances and new challenges in the use of the proper generalized decomposition for solving multidimensional models. *Arch Comput Meth Eng*. 2010;17(4):327-350.
31. Chinesta F, Ladevèze P, Cueto E. A short review on model order reduction based on proper generalized decomposition. *Arch Comput Meth Eng*. 2011;18:395-404.
32. Chinesta F, Keunings R. *Leygue A. The Proper Generalized Decomposition for Advanced Numerical Simulations*: Springer International Publishing; 2014.
33. Ladevèze P. On reduced models in nonlinear solid mechanics. *Eur J Mech A Solids*. 2016;60:227-237.
34. Chamoin L, Allier PE, Marchand B. Synergies between the constitutive relation error concept and PGD model reduction for simplified V&V procedures. *Adv Model Simul Eng*. 2016;3:18.
35. Ladevèze P, Chamoin L. On the verification of model reduction methods based on the proper generalized decomposition. *Comput Meth Appl Mech Eng*. 2011;200:2032-2047.
36. Ladevèze P, Chamoin L. *Toward Guaranteed PGD-reduced Models*. In: Zavarise G, Boso DP, eds. *CIMNE*. Barcelona: Bytes & Science; 2012.
37. Allier PE, Chamoin L, Ladevèze P. Proper generalized decomposition computational methods on a benchmark problem: introducing a new strategy based on constitutive relation error minimization. *Adv Model Simul Eng Sci*. 2015;2(17).
38. Ladevèze P, Moës N, Douchin B. Constitutive relation error estimators for (visco)plastic finite element analysis with softening. *Comput Meth Appl Mech Eng*. 1999;176:247-264.
39. Fraeijs de Veubeke B, Hugge MA. Dual analysis for heat conduction problems by finite elements. *Int J Numer Methods Eng*. 1972;5(1):65-82.
40. Oden JT, Reddy JN. On dual complementary variational principles in mathematical physics. *Int J Eng Sci*. 1974;12:1-29.
41. Fraeijs de Veubeke B. Displacement and equilibrium models in the finite element method. *Int J Numer Methods Eng, Classical Reprint Series*. 2001;52:287-342.
42. Moitinho de Almeida JP, Maunder EAW. *Equilibrium Finite Element Formulations*. New York: Wiley; 2017.
43. Ladevèze P, Rougeot P. New advances on a posteriori error on constitutive relation in finite element analysis. *Comput Meth Appl Mech Eng*. 1997;150:239-249.
44. Babuška I, Strouboulis T, Upadhyay C. S, Gangaraj SK, Copps K. Validation of a posteriori error estimators by numerical approach. *Int J Numer Methods Eng*. 1994;37(7):1073-1123.

45. Ladevèze P, Gastine JL, Marin P, Pelle JP. Accuracy and optimal meshes in finite element computation for nearly incompressible materials. *Comput Meth Appl Mech Eng*. 1992;94(3):303-314.
46. Ammar A, Huerta A, Leygue A, Chinesta F, Cueto E. Parametric solutions involving geometry: a step towards efficient shape optimization. *Comput Meth Appl Mech Eng*. 2014;268(1):178-193.
47. Zlotnik S, Díez P, Modesto D, Huerta A. Proper generalized decomposition of a geometrically parametrized heat problem with geophysical applications. *Int J Numer Methods Eng*. 2015;103(10):737-758.
48. Courard A, Néron D, Ladevèze P, Ballère L. Integration of PGD-virtual charts into an engineering design process. *Comput Mech*. 2016;57(4):637-651.
49. Canuto C, Kozubek T. A fictitious domain approach to the numerical solution of PDEs in stochastic domains. *Numerische Mathematik*. 2007;107(2):257-293.
50. Nouy A, Chevreuil M, Safatly E. Fictitious domain method and separated representations for the solution of boundary value problems on uncertain parameterized domains. *Comput Meth Appl Mech Eng*. 2011;200:3066-3082.
51. Nouy A. A priori model reduction through proper generalized decomposition for solving time dependent partial differential equations. *Comput Meth Appl Mech Eng*. 2010;199:1603-1626.
52. Ammar A, Chinesta F, Díez P, Huerta A. An error estimator for separated representations of highly multidimensional models. *Comput Meth Appl Mech Eng*. 2010;199(25-28):1872-1880.
53. Moitinho de Almeida JP. A basis for bounding the errors of proper generalised decomposition solutions in solid mechanics. *Int J Numer Methods Eng*. 2013;94(10):961-984.
54. Florentin E, Gallimard L, Pelle JP. Evaluation of the local quality of stresses in 3d finite element analysis. *Comput Meth Appl Mech Eng*. 2002;191:4441-4457.
55. Pled F, Chamoin L, Ladevèze P. An enhanced method with local energy minimization for the robust a posteriori construction of equilibrated stress fields in finite element analyses. *Comput Mech*. 2012;49:357-378.
56. Hild F, Bouterf A, Chamoin L, et al. Toward 4D mechanical correlation. *Adv Model Simul Eng Sci*. 2016;3(17).